electronics

MDPI

Review

Propagation Models for Wireless Sensor Networks, Re-Evaluation and Updates

Andreas Giannakoulas, Nikolaos Karkanis, Ioannis Gavriilidis and Theodoros N. F. Kaifas *

Department of Electrical and Computer Engineering, Democritus University of Thrace, 67100 Xanthi, Greece; angiannak@ee.duth.gr (A.G.); nkarkani@ee.duth.gr (N.K.); ioangavr1@ee.duth.gr (I.G.)
* Correspondence: tkaifas@ee.duth.gr

Abstract

Wireless sensor networks are expanding across nearly all aspects of social and economic activity. Their deployment now spans almost all available environments, including, in some cases, off-planet applications. Applications may range from near-ground, underground, undersea, indoor–outdoor, and on- and in-body, to name a few deployment environments. Each channel model exhibits its own physical representation and statistical distributions. In this work, we categorize and re-evaluate the various propagation models published in the open literature while, at the same time, we contribute critical updates needed due to the rapid expansion of the wireless sensor network discipline. Our work includes various results, based on simulation and/or analytical formulas, that advocate for and evaluate our classification and findings. Unlike prior reviews that treat environments in isolation, this article introduces a unified analytical and simulation framework for a cross-environment comparison, with updated parameterizations aligned with modern WSN deployments. The innovation lies in the consistent cross-environment evaluation of propagation mechanisms, updated parameterizations aligned with modern WSN deployments, and the identification of feasibility and trade-off boundaries across heterogeneous media.

Keywords: UGSN; SWSN; BAN

1. Introduction

The rapid evolution of wireless communication technologies, driven by the deployment of fifth- and sixth-generation (5G/6G) networks, is enabling new paradigms in data transmission, processing, and connectivity. These networks are characterized by high data rates, reduced end-to-end latency, and support for massive device connectivity, enabling large-scale wireless sensor network (WSN) deployments. As a result, WSNs are increasingly considered a key enabling technology for distributed sensing and monitoring applications across a wide range of domains.

Advances in microelectronics have led to smaller, more energy-efficient, and cost-effective integrated circuits, facilitating the development of compact and low-power sensor nodes. Such nodes can be deployed in diverse environments, including industrial facilities, agricultural fields, urban infrastructure, and biomedical applications. By enabling continuous monitoring and real-time data exchange, WSNs improve system awareness, early detection of abnormal conditions, and enhanced operational safety. Figure 1 summarizes a classification of sensors by measurement domain [1].

Check for updates

Academic Editor: Adão Silva

Received: 29 December 2025
Revised: 9 February 2026
Accepted: 12 February 2026
Published: 25 February 2026

Copyright: © 2026 by the authors. Licensee MDPI, Basel, Switzerland. This article is an open access article distributed under the terms and conditions of the Creative Commons Attribution (CC BY) license.

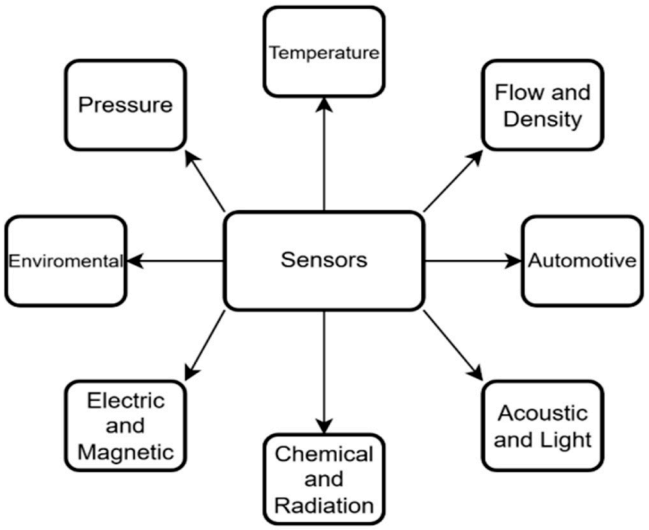

Figure 1. Fundamental sensor types and their measurement domains.

Despite significant progress in hardware integration and communication protocols, several fundamental challenges remain. In many practical scenarios, sensor nodes are deployed in environments that are inaccessible or difficult to service, such as underground structures, submerged regions, or those within biological tissues. In these cases, maintenance, battery replacement, or physical reconfiguration may be impractical or impossible. Consequently, the reliability and predictability of the wireless communication channel become critical factors for ensuring long-term and accurate data delivery. A thorough understanding of electromagnetic wave propagation and channel behavior in such complex media is therefore essential for the design of robust and energy-efficient WSN systems.

This paper presents a comprehensive review of wireless sensor network operation across a range of propagation environments, with an emphasis on the physical characteristics that govern electromagnetic signal transmission and the modeling approaches used to describe them. Figure 2 summarizes the principal categories of deployment environments considered in this work, including indoor, outdoor, underground, submerged, and in-body scenarios. Each environment introduces distinct constraints related to material properties, propagation losses, multipath effects, and energy consumption. In addition to the theoretical discussion, simulation results are presented to evaluate channel performance under representative environmental conditions, providing insight into achievable communication ranges and energy efficiency limits. The remainder of the paper is organized as follows.

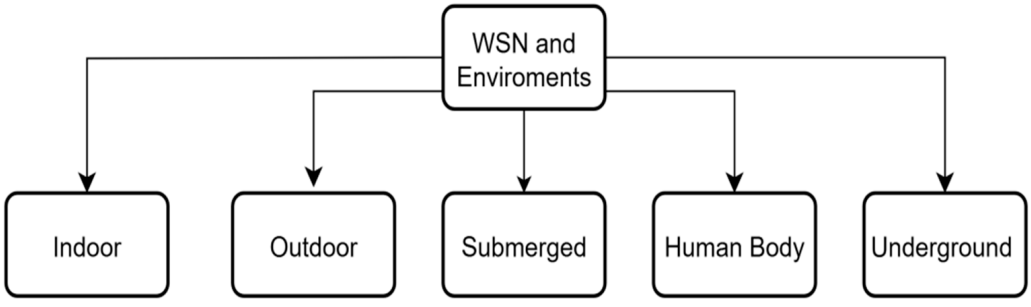

Figure 2. Classification of wireless sensor network (WSN) deployment environments.

The main contributions of this work can be summarized as follows:

(i) A unified analytical and simulation-based framework is presented for the comparative evaluation of electromagnetic propagation models in wireless sensor networks across

heterogeneous deployment environments, including underground, submerged, in-body, indoor, and outdoor scenarios.

(ii) Classical and state-of-the-art propagation models reported in the literature are systematically re-evaluated and updated, with an emphasis on parameterizations relevant to modern WSN and IoT deployments, operating from sub-GHz to millimeter-wave frequency bands.

(iii) Consistent performance metrics and modeling assumptions are employed across fundamentally different propagation media, enabling direct cross-environment comparison in terms of path loss, achievable range, energy efficiency, and feasibility limits.

(iv) Representative analytical and simulation results are provided to highlight dominant physical mechanisms, sensitivity to environmental parameters, and trade-offs between the communication modality, frequency selection, and deployment conditions.

This unified treatment offers a structured reference for researchers and practitioners seeking to select, compare, and adapt propagation models for diverse and emerging wireless sensor network applications.

Methodology and Research Framework

This work follows a structured review and comparative analysis methodology aimed at enabling the consistent evaluation of wireless sensor network (WSN) propagation models across heterogeneous deployment environments. First, representative propagation environments are identified based on physical domain characteristics, including underground, submerged, body-centric, indoor, and outdoor scenarios. For each environment, established analytical, empirical, and semi-empirical propagation models are selected from the open literature, prioritizing models that have been experimentally validated and widely adopted in WSN and IoT research.

Second, the selected models are harmonized through consistent assumptions regarding antenna characteristics, operating frequency ranges, and performance metrics such as path loss, achievable range, and energy efficiency. Where applicable, updated parameterizations reflecting modern WSN deployments are incorporated. Analytical expressions are complemented by simulation-based evaluations to quantify performance trends and sensitivity to environmental parameters.

Finally, results are interpreted within a unified comparative framework, allowing a direct cross-environment assessment of propagation feasibility and trade-offs. The methodology emphasizes a relative performance comparison rather than absolute optimization, enabling systematic insight into the suitability of different communication mechanisms for specific deployment scenarios.

2. Development Scenarios for Wireless Sensor Networks: Physical Domains and Design Implications

In the current section we elaborate, with detail,

- on underground and submerged (Section 2.1),
- on- and in-body (Section 2.2), and
- out- and indoor (Section 2.3) propagation models for wireless sensor networks.

2.1. Underground and Submerged Wireless Sensor Networks

Wireless sensor networks deployed underground or in submerged environments operate under severe propagation constraints characterized by high attenuation, strong material losses, and non-line-of-sight conditions. Such networks are essential in applications including precision agriculture, mining, underground infrastructure monitoring, environmental sensing, and marine observation systems. Unlike conventional terrestrial

radio frequency (RF) communication, these environments require specialized propagation models that account for lossy media and complex boundary interactions.

2.1.1. Underground Wireless Sensor Networks (UGSNs)

Underground wireless sensor networks (UGSNs) are increasingly employed in applications such as precision agriculture, underground infrastructure monitoring, environmental sensing, seismic activity observation, and mineral exploration. In these systems, sensor nodes are either fully buried in soil or installed at shallow depths and are typically required to communicate over non-line-of-sight (NLOS) paths through heterogeneous and electrically lossy media. As a result, underground propagation is fundamentally different from conventional terrestrial wireless communication and requires dedicated modeling approaches.

Electromagnetic wave propagation in underground environments is dominated by high attenuation, frequency-dependent dielectric losses, and strong sensitivity to the soil composition. As illustrated in Figure 3, the physical properties of soil, particularly the relative proportions of sand, silt, clay, and organic matter, directly determine the effective complex permittivity of the medium and, consequently, the attenuation and phase velocity of propagating signals. The soil moisture content is a critical factor, as an increased water concentration substantially raises both permittivity and electrical conductivity, leading to significantly higher propagation losses.

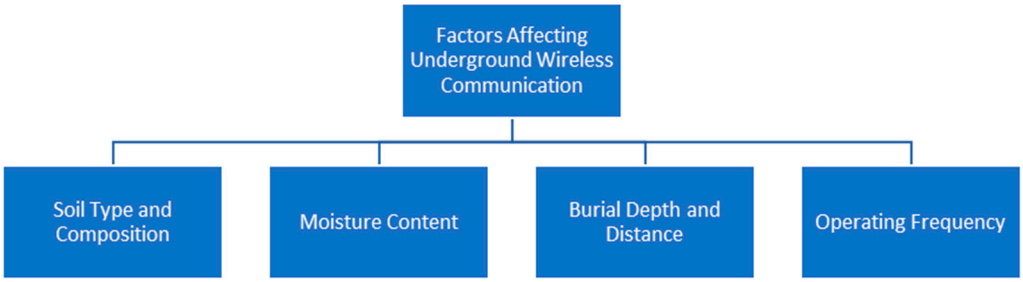

Figure 3. Key factors affecting underground wireless communication.

In addition, the burial depth of sensor nodes and the horizontal separation distance introduce degradation effects that cannot be captured by free-space models. The operating frequency further influences signal penetration, with lower frequencies generally offering improved propagation through soil at the cost of reduced available bandwidth and data rates. These coupled dependencies highlight the need for accurate, environment-aware propagation models in the design and deployment of UGSNs [2–4], (see Figure 4).

2.1.2. Propagation Models in UGSNs

Propagation models for underground wireless sensor networks can be broadly classified into two categories: far-field electromagnetic models, which operate in radiative regimes at relatively high frequencies, and near-field models, which are typically associated with quasi-static operation at lower frequencies. This distinction reflects fundamentally different physical propagation mechanisms and leads to markedly different path-loss characteristics.

Underground Far-Field EM propagation Models: Recent studies have provided extensive insight into the modeling and prediction of electromagnetic (EM) wave propagation in underground wireless sensor networks (UGSNs) [5,6]. In radiative regimes, signal attenuation is commonly modeled using extensions of free-space propagation formulas that explicitly account for the lossy nature of soil. Among these, two widely adopted

approaches are the modified Friis model [7] and the Complex Refractive Index Model with Fresnel corrections (CRIM–Fresnel) [8].

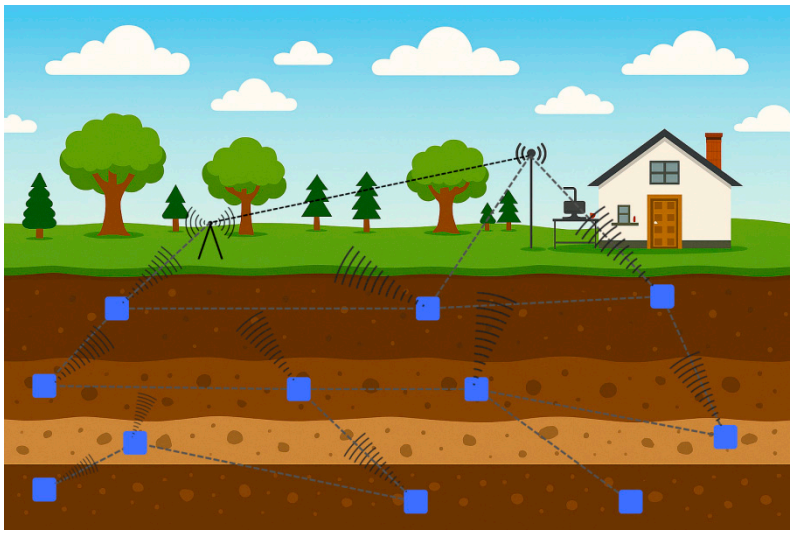

Figure 4. Underground WSN.

The modified Friis model extends the classical Friis transmission equation by incorporating attenuation due to the lossy propagation medium in addition to geometric spreading. In this formulation, signal power decays not only because of angular spreading associated with the expansion of ray tubes, but also due to thermal losses arising from the finite conductivity of soil. These additional losses are typically modeled using concepts borrowed from lossy transmission-line theory, with medium parameters derived from the soil composition and moisture content. As a result, the modified Friis model provides a first-order approximation of underground EM propagation that remains compatible with a conventional link-budget analysis while capturing the dominant attenuation mechanisms introduced by the soil. Ray tube widening is modeled adequately by the free space Friis formula

$$\begin{aligned} \frac{P_{RX}}{P_{TX}} &= \frac{G_{RX}G_{TX}}{L_0} \\ L_0 &= \left(\frac{4\pi d}{\lambda}\right)^2 = (2\beta d)^2 \end{aligned} \tag{1}$$

where P_{RX} and P_{TX} are the received power at the receiver (Rx) and the transmitted power by the transmitter (Tx). G_{RX} and G_{TX} are the antenna gains of the Rx and Tx, respectively, and L_0 represents the losses due to spreading, with λ and β being the wavelength and propagation (imaginary part) and wave number of the surrounding medium and d being the actual distance between Tx and Rx. On the other hand, the losses along the ray trajectory can be modeled assuming propagation along a lossy transmission line, resulting in the use of

$$\frac{P_{RX}}{P_{TX}} = e^{-2\alpha d} = \frac{1}{L_m} \tag{2}$$

where α is the losses exponent (real part of the wave number), and L_m denotes the losses due to the lossy material. Combining the spreading and material losses, the received power is expressed as follows:

$$\begin{aligned} &\frac{P_{RX}}{P_{TX}} = \frac{G_{RX}G_{TX}}{L_0}\frac{1}{L_m} \Rightarrow \\ &P_{RX,dB} = G_{RX,dB} + G_{TX,dB} - L_{0,dB} - L_{m,dB} \\ &L_{0,dB} = 20\log_{10}(2\beta d) \\ &L_{m,dB} = 20\log_{10}(e^1)\alpha d \end{aligned} \tag{3}$$

The propagation is assumed to be held on a complex but isotropic and uniform environment under the following propagation constants and respective wavenumber:

$$\begin{aligned} \alpha &= \omega \sqrt{\frac{\mu\varepsilon'}{2}\left(\sqrt{1+\left(\frac{\varepsilon''}{\varepsilon'}\right)^2}-1\right)} \\ \beta &= \omega \sqrt{\frac{\mu\varepsilon'}{2}\left(\sqrt{1+\left(\frac{\varepsilon''}{\varepsilon'}\right)^2}+1\right)} \\ \gamma &= \alpha - j\beta \end{aligned} \tag{4}$$

In the preceding expressions, μ denotes the magnetic permeability of the soil, which is typically close to the free-space value, while ε' and ε'' represent the real and imaginary parts of the complex dielectric permittivity, respectively. The complex permittivity accounts for both energy storage and conductive losses within the medium. In practice, ε' and ε'' are commonly estimated using empirical dielectric mixing models, such as the one reported in [9], which relate the effective soil permittivity to its physical composition and volumetric water content:

$$\begin{aligned} \varepsilon &= \varepsilon' - j\varepsilon'' \\ \varepsilon' &= 1.15\left(1+\frac{\rho_b}{\rho_s}\cdot\varepsilon^{0.65}+(m_v)^{\overline{\beta}}\cdot\left(\overline{\eta}_{fw}\right)^{0.65}-m_v\right)^{1/0.65}-0.68 \\ \varepsilon'' &= \left((m_v)^{\overline{\overline{\beta}}}\cdot\left(\overline{\overline{\eta}}_{fw}\right)^{0.65}\right)^{1/0.65} \\ \overline{\beta} &= 1.2748-0.519S-0.152C \\ \overline{\overline{\beta}} &= 1.33797-0.603S-0.166C \end{aligned} \tag{5}$$

where m_v is the volumetric water content, ρ_b is the bulk density of the soil given in g/cm^3, and $\rho_s = 2.66$ g/cm^3 is the solid particle density. S and C are the presentence of sand and clay particles and $\overline{\eta}_{fw}(\overline{\overline{\eta}}_{fw})$ is the real (imaginary) part of the relative dielectric constant of the free water.

A related approach is the CRIM–Fresnel model, originally proposed in [8] and further elaborated in [10], which explicitly accounts for the interaction between the transmitting antenna and its immediate surrounding medium. In addition to modeling attenuation due to propagation through soil using a complex refractive index, this model incorporates losses arising from impedance mismatch and reflection at the antenna–soil interface. As a result, the total attenuation is expressed as the combination of propagation-related losses within the soil and reflection losses associated with the transmission boundary.

A critical aspect of the CRIM–Fresnel formulation is that the reflection-related attenuation is not dependent on the propagation path between the transmitter and receiver, but rather on the specific experimental configuration considered in [8]. In that setup, the transmitting antenna was enclosed within an air-filled box that was subsequently buried in soil. The authors modeled the power loss at the transmitter–air–soil transition using an average reflectance factor, as opposed to average transmittance, obtained by incoherently summing multiple power reflections within the enclosure ([11] Example 4.5.3). This treatment captures interface-induced losses associated with the measurement arrangement rather than intrinsic soil propagation effects.

$$\begin{aligned} R_c &= \frac{2R}{1+R} \\ R &= |\Gamma|^2 \end{aligned} \tag{6}$$

with Γ being the (box) air soil reflection coefficient. The total losses, in dBs, read as follows:

$$\begin{aligned} A_{tot} &= ad + 10\log_{10}(R_c) \\ a &= 20\log_{10}(e^1)\alpha \end{aligned} \tag{7}$$

The preceding derivation assumes electromagnetic wave propagation in a homogeneous and uniform medium. When clearly distinguishable material interfaces are present, however, a planar stratified medium approximation may be adopted. For instance, if sensor nodes are located near the ground–air interface (or, equivalently, near the water–air interface), propagation effects associated with boundary reflections become significant and should be explicitly accounted for. In such cases, a geometrical ray-based formulation can be employed, in which the contribution of a reflected ray from the interface is included in addition to the direct propagation path. This approach leads to the well-known two-wave model [12,13].

The geometrical optics (GO) framework represents a high-frequency approximation of Maxwell's equations, formally valid in the limit $\omega \to \infty$, where electromagnetic energy is assumed to propagate along rays or, more precisely, along ray tubes with a varying cross-sectional area. Within this approximation, the conservation of energy is enforced over expanding ray tubes, while the propagation paths satisfy Fermat's principle of least time.

Beyond the two-wave formulation, an additional field component known as the lateral wave may be included [14]. Accounting for this contribution yields the three-wave model, as presented in [15]. This model considers a ray system comprising direct, reflected, and lateral propagation paths, as illustrated in Figure 5. For each path, expressions for the power density incident at the receiver are derived and subsequently multiplied by the equivalent receiving aperture of the antenna to compute the total received power.

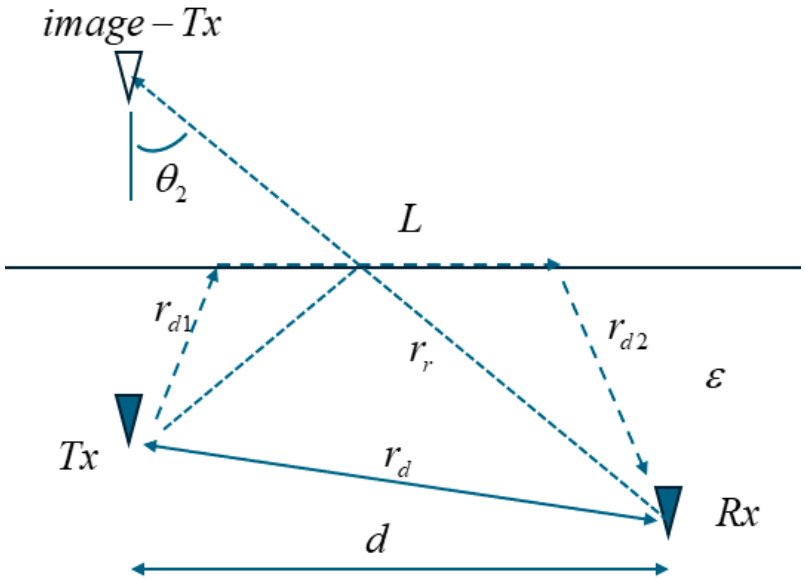

Figure 5. The three-wave model.

We enlist here the relative equations (which have been corrected so that the average pointing vector is a real quantity), for completeness.

$$\begin{aligned} P_{av}^{d} &= \left(\frac{D_d}{4\pi {r_1}^2}\right) e^{-2ar_1} G_t = \left(\frac{D_d}{4\pi {r_d}^2}\right) e^{-2ar_d} G_t \\ P_{av}^{r} &= \left(\frac{D_r}{4\pi {r_2}^2}\right) e^{-2ar_2} G_t \Gamma^2 = \left(\frac{D_r}{4\pi {r_r}^2}\right) e^{-2ar_r} G_t \Gamma^2 \\ P_{av}^{r} &= \left(\frac{D_l}{4\pi d^4}\right) e^{-2a(h_t+h_r)} e^{-2a_o d} G_t T^2 = \left(\frac{D_l}{4\pi d^4}\right) e^{-2a(r_{d1}+r_{d2})} e^{-2a_o L} G_t T^2 \end{aligned} \tag{8}$$

In the previous, D_d, D_r, and D_l are constant parameters given in [15]. Also, r_d is the direct Tx-Rx distance, while r_r is the direct Tx image-Rx distance (where Tx-image is the Tx mirror point with respect to the interface). Γ and T are the reflection and transmission coefficients, respectively. Finally, r_{d1}, r_{d2}, L are presented in Figure 5. To compute the received power, one needs to multiply the sum of the previous with the receiving antenna's equivalent area defined as

$$A = \left(\frac{\lambda^2}{4\pi}\right) G_r \tag{9}$$

This model can be farther elaborated by using more accurate formulas that take into account second-order phenomena that are nevertheless dominant in cases that might be beneficial to the communication link. In the current work, we reconstruct the three-ray model by using the induced open circuit Voltage at the Rx to compute the received power. For the examined case, it reads as follows [16] (Chapter 5.5):

$$\begin{aligned} V_{oc} &= V_{oc}^d + V_{oc}^r + V_{oc}^l = -\vec{h}^{\,d}_{RX} \cdot \vec{E}^{\,d} - \vec{h}^{\,r}_{RX} \cdot \vec{E}^{\,r} - \vec{h}^{\,l}_{RX} \cdot \vec{E}^{\,l} \\ \vec{E}^{\,d} &= -\gamma Z_{\mathrm{TX}} \tfrac{e^{-\gamma r_d}}{4\pi r_d} I_{TX} \vec{h}^{\,d}_{TX} \\ \vec{E}^{\,r} &= -\gamma Z_{\mathrm{TX}} \tfrac{e^{-\gamma r_r}}{4\pi r_r} \Gamma I_{TX} \vec{h}^{\,r}_{TX} \\ \vec{E}^{\,l} &= -\gamma Z_{\mathrm{TX}} \cdot U(L) \left(\tfrac{2n^4}{(1+n^2)(1-n^4)} \right) F(v) \tfrac{e^{-\gamma(r_{d1}+r_{d2})} e^{-\gamma L}}{4\pi\rho_d} I_{TX} \vec{h}^{\,l}_{TX} \end{aligned} \tag{10}$$

Previous equations draw heavily on [17] and result from a nonuniform saddle point evaluation of the respective Sommerfeld integral using the Van der Wearden approach [18]. $\vec{h}^{\,d,r,l}_{TX}$ ($\vec{h}^{\,d,r,l}_{RX}$) is the TX (RX) equivalent radiation vector for the direct, reflected, and lateral paths. γ, n, Z_{TX} are the propagation medium's wavenumber, refractive index, and intrinsic impedance, while I_{TX} is the current of the transmitter and U is the step function. Function F is Sommerfeld's attenuation function, and variable v is the numerical distance [19], both presented in the following equation:

$$\begin{aligned} &F(v) = 1 - j\sqrt{\pi v} e^{-v} erfc(j\sqrt{v}) \\ &v = jr_r k\left(\cos(\gamma_p - \theta_2) - \cos(\gamma_b - \theta_2)\right) \\ &\cos(\gamma_p) = \tfrac{1}{\sqrt{1+n^2}}; \sin(\gamma_p) = \tfrac{n}{\sqrt{1+n^2}} \\ &\gamma_b = \sin^{-1}(n) \end{aligned} \tag{11}$$

γ_p and γ_b are the Sommerfeld pole and the branch-cut point of the propagating environment, respectively. The main outcome, that those relations present, is the fact that for receiver positions close to the interface, between near-field (where the losses are about -60 dB/dec) and far-field (where the losses are -40 dB/dec), there is a propagation area (between ρ_l (the behavior change point at the end of near-field range) and $\rho_r = \left(2real(\gamma)\left|\frac{1}{\sqrt{1+n^2}} - 1\right|\right)^{-1}$ (the behavior change point at the start of the far-field (see Tables 1 and 2 of [17])), where the attenuation is milder and equal to -20 dB/dec. This is due to the fact that the Sommerfeld's attenuation function has an asymptotic behavior, given next.

$$F(v) = \begin{pmatrix} 1 & v \to 0 \\ -1/(2v) & v \to +\infty \end{pmatrix} \tag{12}$$

Furthermore, this model can be extended to provide results in case Tx and Rx are in different layers (under-overground, under-over sea), applying the concept of refraction [20]. In this way, one can obtain the communication link characteristics of different types of WUSN channels such as the underground to underground (UG–UG) channel, underground to above-ground (UG–AG) channel, and above-ground to underground (AG–UG) channel.

Indeed, in case Tx and Rx are in different layers, one can replace the reflection coefficient with a generalized refraction coefficient to obtain first-order approximate results.

An analogous condition (to the milder due to lateral wave propagation losses) worth mentioning is the case of near-ground propagation [21]. Then, when the so-called pole dominance condition is respected,

$$\frac{\left|n^2\right|}{\left|k_1(n(h_t+h_r)+jk_1h_th_r)\right|} > 1 \tag{13}$$

(for $\left|n^2\right| > 10$ and from $\rho_{\min} \sim n(h_t+h_r)$ to $\rho_{break} \sim 2\left|n^2\right|/k_1$); the propagation is mainly due to the pole (which is originated by the so—called Norton's ground wave and especially its Zenneck wave component), and

$$\vec{E}^{r}_{pole} = -\gamma Z_{TX}\frac{e^{-\gamma r_r}}{4\pi r_r} I_{TX}\vec{h}^{r}_{TX}F(v) \sim \frac{e^{-\gamma r_r}}{\sqrt{r_r}} \tag{14}$$

So, under conditions, this term has the potential to produce -20 dBs/dec, which is highly desirable.

In the previous comprehensive formulations, in addition to the direct and reflected waves, a third field component is taken into account, physically originated by the diffraction at the interface of the two media. In the case RX is close to the interface, if it is buried (or submerged) in the denser medium, one should take into account the lateral wave produced by the branch-cut and Sommerfeld-pole-initiated field component. If RX is outside the denser medium then this, diffraction due to the interface-originated, component, and ignored by ray-based techniques can become predominant and stimulate the near-ground propagation. Efforts to harvest those phenomena are presented in [22,23]

Underground Near-Field EM propagation Models: Complementary to radiative, far-field–based approaches, near-field propagation models have been proposed for underground wireless sensor networks, motivated by the fact that severe attenuation in lossy media often prevents the establishment of a true far-field regime. This class of models primarily encompasses magnetic induction (MI)-based channel formulations [23], which operate in the quasi-static near-field region.

In the near field, the electric and magnetic field components are not coupled through a constant wave impedance, and their spatial decay characteristics differ from those of propagating plane waves. Consequently, near-field behavior depends separately on the dielectric properties of the medium (affecting the electric field) and the magnetic properties (affecting the magnetic field). This distinction is particularly relevant in underground environments, where wireless links experience strong attenuation due to propagation through soil, rock, and moisture-rich media.

Magnetic-induction-based transmission has therefore been proposed as a viable alternative for short-range underground communication, as magnetic fields are generally less sensitive to variations in dielectric permittivity than electric fields. While most natural soils exhibit a relative magnetic permeability close to that of free space, MI links are nevertheless affected by conductive losses, eddy-current dissipation, and reductions in coil quality factor induced by the surrounding medium [24,25]. Despite these limitations, MI-based techniques offer improved robustness and predictability compared to radiative EM propagation in highly lossy underground environments.

A model for magnetic induction is based on the field produced by a magnetic Hertz dipole [11] (extracted via duality for the respective electrical Hertzian dipole):

$$\begin{aligned}
&\vec{E}(\vec{r}) = j\omega\mu_0\gamma^2\left(1+\tfrac{1}{\gamma r}\right)\left(\hat{r}\times\vec{m}_{TX}\right)G(\vec{r})\\
&\vec{H}(\vec{r}) = \gamma^3\left(1+\tfrac{1}{\gamma r}\right)\left(\frac{3\hat{r}\left(\hat{r}\cdot\vec{m}_{TX}\right)-\vec{m}_{TX}}{\gamma r}\right)G(\vec{r}) - \gamma^2\hat{r}\times\left(\vec{m}_{TX}\times\hat{r}\right)G(\vec{r})\\
&G(\vec{r}) = \tfrac{e^{-\gamma r}}{4\pi\gamma r}\\
&\vec{m}_{TX} = j\omega\mu N_{TX}S_{TX}\hat{z}
\end{aligned} \tag{15}$$

In Equation (15), N denotes the number of turns of the transmitting coil, S is the effective area of the coil, ω is the angular frequency of operation, and μ represents the magnetic permeability of the surrounding medium. These parameters jointly determine the strength of the generated magnetic field and the resulting coupling between the transmitting and receiving coils in the magnetic induction channel.

Assuming near-field ($\gamma r \to 0$), expanding in inverse γr, and retaining the larger terms $(1/(\gamma r)^3)$, previous equations read as follows:

$$\begin{aligned}
&\vec{E}(\vec{r}) \cong 0\\
&\vec{H}(\vec{r}) \cong \gamma^3\left(\tfrac{1}{\gamma r}\right)\left(\frac{3\hat{r}\left(\hat{r}\cdot\vec{m}_{TX}\right)-\vec{m}_{TX}}{\gamma r}\right)G(\vec{r}) = m_{TX}\gamma^3\left(\tfrac{1}{\gamma r}\right)\left(\tfrac{2\hat{r}\cos\theta-\hat{\theta}\sin\theta}{\gamma r}\right)G(\vec{r})
\end{aligned} \tag{16}$$

In the last equation we assumed $\vec{m}_{TX} = m_{TX}\hat{z}$. The induced electromotive voltage at the receiver coil, after using Faraday's law in the integral form, reads as follows:

$$V^{ind} = \vec{m}_{RX}\cdot\vec{H} = \vec{m}_{RX}\cdot\left(m_{TX}\gamma^3\left(\frac{1}{\gamma r}\right)\left(\frac{2\hat{r}\cos\theta-\hat{\theta}\sin\theta}{\gamma r}\right)G(\vec{r})\right) \tag{17}$$

In the preceding expression, it is noted that the received power P_r exhibits a sixth-power dependence on the normalized transmitter–receiver separation, reflecting the characteristic r^{-6} decay of magnetic induction links in the quasi-static near-field regime. This strong distance dependence fundamentally limits the achievable communication range of MI-based systems.

To mitigate this limitation and extend coverage, several enhancement strategies have been proposed. These include the exploitation of randomly distributed buried conductive objects and the deployment of intentional passive repeaters, which can improve magnetic coupling along the propagation path [26]. In addition, guided or waveguide-like structures implemented underground or underwater have been investigated as a means of supporting controlled energy transport with reduced radiation loss [27,28]. Such approaches can offer advantages in terms of low transmit power requirements and predictable channel behavior, while largely avoiding multipath fading and Doppler effects that are typical of radiative propagation mechanisms.

2.1.3. Design Considerations for UGSNs

In the design of underground wireless sensor network (UGSN) models, achieving an appropriate balance between model accuracy and computational complexity is essential, particularly for real-time or resource-constrained applications. Beyond propagation modeling, several practical system-level factors significantly influence overall network performance.

The antenna type, polarization, and orientation play a critical role in determining the link quality, as the interaction between the radiating structure and the surrounding soil

strongly affects coupling efficiency and attenuation. In many underground deployments, horizontally oriented antennas have been reported to provide improved performance compared to vertical configurations, depending on the burial depth and soil stratification.

Communication protocols also require adaptation to account for the characteristics of underground channels. In particular, medium access control (MAC) strategies must be designed to tolerate high path loss, increased latency, and intermittent connectivity. Furthermore, environmental dynamics such as seasonal rainfall, irrigation, or long-term soil moisture variations can significantly alter the electrical properties of the propagation medium. As a result, adaptive modeling and parameter updating are often necessary to maintain reliable network operation over time.

Overall, underground WSN propagation modeling constitutes a multidisciplinary challenge that integrates concepts from electromagnetic theory, geophysics, and environmental science, underscoring the need for cross-domain approaches in the design and deployment of UGSNs.

2.1.4. Submerged Wireless Sensor Networks (SWSNs)

Submerged wireless sensor networks (SWSNs), see Figure 6, are designed for deployment in aquatic and marine environments and play a critical role in applications such as oceanographic data collection, offshore infrastructure monitoring, environmental observation, and disaster detection (e.g., tsunami early-warning systems). In contrast to terrestrial and underground scenarios, the underwater propagation medium imposes severe constraints on wireless communication due to the inherently high attenuation of electromagnetic (EM) waves, particularly in conductive seawater.

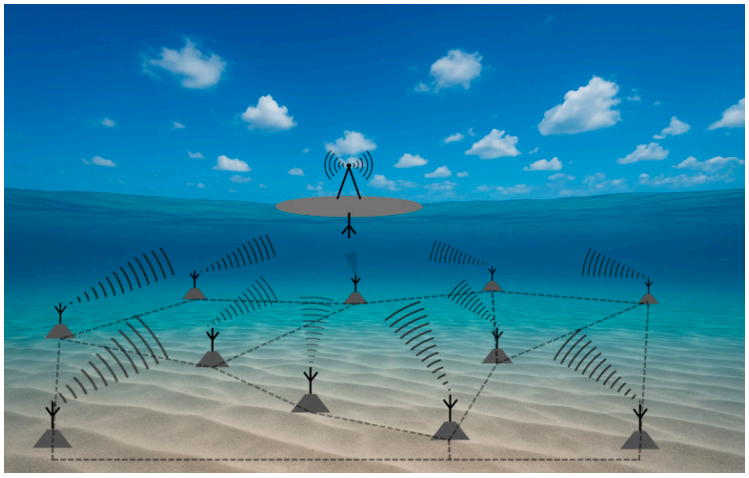

Figure 6. Submerged WSN.

As a result, the communication range, energy efficiency, and achievable data rates in SWSNs are strongly limited by the electrical properties of the surrounding medium, necessitating specialized channel models and system designs tailored to submerged environments.

2.1.5. Communication Modalities in SWSNs

Communication in submerged wireless sensor networks is primarily constrained by the strong attenuation of electromagnetic waves in water, particularly in conductive seawater. Within this section, we review electromagnetic, magnetic-induction, optical, and acoustic channel models relevant to submerged WSNs, highlighting the operational regimes where each modality is feasible.

Electromagnetic (EM) Communication: Electromagnetic wave propagation in water is severely limited by the medium's electrical conductivity, which leads to rapid exponential

attenuation, especially at higher frequencies. Consequently, EM-based communication in submerged environments is typically restricted to short distances and low frequencies. Nevertheless, EM links can be effective for very short-range, high-data-rate communication, particularly in freshwater, low-salinity conditions, or shallow-water deployments where attenuation is comparatively reduced.

Magnetic-induction-based communication has emerged as a robust alternative for short-range submerged links. MI techniques rely on quasi-static magnetic field coupling between transmitter and receiver coils and are therefore less sensitive to variations in water turbidity, salinity, and temperature compared to radiative EM propagation. While MI communication remains fundamentally range-limited due to its near-field nature, it offers improved channel stability, predictable attenuation behavior, and enhanced reliability in both freshwater and seawater environments, making it well suited for short-range submerged sensing applications [4].

2.1.6. Propagation Models and Literature

Several classical and modern models have been developed to characterize signal propagation in submerged environments under electromagnetic and magnetic-induction-based communication paradigms [29,30]. Many of the fundamental modeling principles discussed in the previous section for underground wireless sensor networks, including propagation in lossy media and near-field coupling mechanisms, are directly applicable to submerged scenarios when the electrical properties of water are properly incorporated.

In submerged environments, electromagnetic wave propagation is primarily governed by the complex permittivity of the medium, which is strongly influenced by the conductivity, salinity, and temperature. Compared to soil, seawater exhibits significantly higher electrical conductivity, resulting in larger attenuation constants and severely reduced penetration depths. Consequently, far-field electromagnetic propagation in submerged environments is typically limited to very short communication distances and is mainly relevant in freshwater or shallow-water conditions.

Near-field magnetic-induction-based models play a central role in submerged wireless sensor networks. Similar to underground environments, MI propagation relies on quasi static magnetic field coupling between transmitter and receiver coils and can be accurately described using magnetic dipole formulations adapted to the electromagnetic properties of water. Although the achievable range remains constrained by the characteristic sixth power distance dependence of near-field coupling, MI-based links offer improved robustness and predictable attenuation behavior in submerged environments, as they are less sensitive to conductivity variations than radiative electromagnetic waves.

Overall, propagation modeling for submerged wireless sensor networks within the electromagnetic and magnetic induction framework closely parallels underground propagation modeling, with the primary distinction arising from the higher conductivity and the relative homogeneity of aquatic media. These characteristics necessitate careful selection of the operating frequency, coil geometry, and deployment range to ensure reliable short-range submerged communication.

The exponent part of the Beer–Lambert Law divided by the ray traveled distance is the total attenuation coefficient given by

$$c(\lambda) = a(\lambda) + b(\lambda) \tag{18}$$

where a denotes the total absorption coefficient and b the total scattering coefficient whose values are compiled, for example, in [31] for various standard water types [32]. Respective formulas (with respect to wavelength, temperature and salinity) are also published for the

sea water refractive index [33]. The previous concepts and factors, for a LoS optical path, are lumped into the following model [34–37].

$$\begin{aligned} P_{RX} &= P_{TX}\eta_{TX}\eta_{TX}G_{RX}^{LoS}\chi(\psi_{ij})\exp\left(-c(\lambda)\frac{d_{TX-RX}}{\cos(\varphi_{TX-RX})}\right) \\ G_{TX-RX}^{LoS} &= \begin{cases} \frac{A_{RX}}{d_{TX-RX}^2}\frac{\cos(\varphi_{TX-RX})}{2\pi(1-\cos(\theta_{TX}))} & -\pi/2 \le \varphi_{TX-RX} \le \pi/2 \\ 0 & otherwise \end{cases} \\ \chi(\psi_{RX}) &= \begin{cases} \frac{n^2}{\sin^2(\Psi_{RX}))} & 0 \le \psi_{RX} \le \Psi_{RX} \\ 0 & \varphi_{RX} > \Psi_{RX} \end{cases} \end{aligned} \tag{19}$$

In the previous, P_{RX}, (P_{TX}) is the received (transmitted) power and η_{TX}, (η_{TX}) Tx (Rx) efficiency. d_{TX-RX} is the perpendicular distance between Tx and Rx planes, φ_{TX-RX} is the angle between the normal to the perpendicular to the Rx plane and the Tx-Rx trajectory, A_{RX} is the receiver aperture area, θ_{TX} is the laser beam divergence angle, $\chi(\psi_{ij})$ is the concentrator's gain in case of non-imaging concentrators [38], ψ_{RX} is the angle of incidence with respect to the concentrator axis, and Ψ_{RX} is the concentrator's Field of View. G_{TX-RX}^{LoS} is the link gain in case of LoS. For NLoS, the respective gain can be found in [39], while for Retroreflective links (similarly to backscatter communication in RF systems), retro-reflective optical communication consists of a light source and a reflector, in [40].

The previous equation is a deterministic and static one where all the variations due to fluctuation of the environment (i.e., turbulence, or variations in water salinity or temperature) are neglected. Alternatively, and in order to increase accuracy of the model, one can add a stochastic flavor [41,42], as follows. Assuming x as the sampled baseband signal transmitted by TX and y as the respective signal at the RX for a (using wireless communications nomenclature), a flat (slow) single-input single-output baseband fading channel we get the following:

$$y = h \cdot x + n \tag{20}$$

n is the additive white Gaussian noise (AWGN) for other types of noise, see [43]. And h is the combined channel state that is defined as

$$\begin{aligned} &h = h_a h_t h_p h_{AoA} \\ &h_a = e^{-(a(\lambda)+b(\lambda))L} \\ &h_t(Turbulance) \\ &h_p(\text{pointingError}) \\ &h_{AoA}(\text{AoAfluctations}) \end{aligned} \tag{21}$$

h_a can be considered a deterministic variable defined using a and b of Equation (18). $h_t(Turbulance)$, $h_p(\text{pointingError})$, and $h_{AoA}(\text{AoAfluctations})$ can be considered random variables due to turbulence, pointing error, and AoA fluctuations with *F*, *Hoyt*, and *Rayleigh* probability distribution functions, respectively. Previous models underline the critical role that underwater optical propagation models are to play in underwater communications, since if the relative small ranges problem is alleviated, cutting-edge wireless technology developed for 5G and beyond could be employed [44].

The acoustic channel exhibits multipath components [45]. Multipath is due to reflection at the surface and the bottom and refraction. The refraction is from the spatially non-constant refraction index, meaning from the spatially non-constant speed of sound. Temperature, salinity, and pressure affect the speed of sound, and their variations results in analogous variations in the speed of the acoustic pressure fronts. With the increase in depth, the temperature decreases (in the region called the main thermocline), until it reaches 4 °C, while pressure increases without limit. Those facts result in an initial decrease in the speed

of sound and subsequent increase as the depth increases. Now, it is well known that a ray of sound always bends toward the region of lower propagation speed, obeying Snell's law. A sufficiently accurate formula, for most underwater applications, for the speed of sound is given as follows:

$$c[\mathrm{m/s}] = 1449.2 + 4.6T - 0.055T^2 + 0.00029T^3 + (1.34 - 0.01T)(S - 35) + 0.016z \quad (22)$$

where T is the temperature in °C, S is the salinity in ppt, and z is the depth in m. The formula is valid for 0 °C $\leq T \leq$ 35 °C, 0 ppt $\leq S \leq$ 45 ppt, and 0 m $\leq z \leq$ 1000 m. The previous equation reveals that there is a depth where the sound speed is minimum. At this depth, the sound propagation tends to be focused. This channel is known as the Sound Fixing and Ranging (SOFAR) channel, and there, very long-range propagation (analogous to the propagation in graded-index optical fibers) is possible. In any case, this acoustic speed variation results in rays bending and forming almost periodic patterns of lit and shadow regions, signifying the complexity that characterizes the acoustic underwater propagation.

For a single, say the p-th, path, the overall propagation loss of the respective acoustic channel is due to absorption (where acoustic energy is transformed into heat) and spatial spreading (where the acoustic front is expanding to cover the available space):

$$\begin{aligned} A(l,f) &= \left(\tfrac{l}{l_r}\right)^k a(f)^{(l-l_r)} = l^k a(f)^l \\ a(f) &= 0.0033 + \tfrac{0.11f^2}{1+f^2} + \tfrac{44f^2}{4100+f^2} + 0.0003f^2 \end{aligned} \quad (23)$$

In the previous, f stands for the frequency in kHz, and l/l_r is the ratio of the Tx-Rx distance divided by some reference one. The exponent k takes values that are between 1 and 2 (for cylindrical and spherical spreading, respectively). The absorption coefficient $a(f)$ can be obtained using an empirical formula (there are various choices like the Thorp formula, Schulkin and Marsh formula, and Francois and Garrison formula) [46,47].

Focusing on long-range propagation, the propagating ray-tube of the p-th path reflects on the sea surface and sea floor multiple times and the respective transfer function reads as follows [48]:

$$\begin{aligned} H_p(f) &= \frac{\Gamma_p}{\sqrt{A(l,f)}} \Rightarrow \\ H(f) &= \sum_p H_p(f) e^{-2\pi f \tau_p} = \sum_p \frac{\Gamma_p}{\sqrt{A(l,f)}} e^{-2\pi f \tau_p} \end{aligned} \quad (24)$$

τ_p is the relative delay of the p-th path. The cumulative reflection coefficient is the product of the respective reflection coefficients that in the sea surface is well approximated by -1 and for the bottom can be found in [47] (Chapter 3). This means that the overall transfer function is a sum over a series of low-pass filters. The respective overall impulse response reads as follows:

$$h(t) = \sum_p h_p(\tau - \tau_p) \quad (25)$$

where $h_p(t)$ is the inverse Fourier Transform of $H_p(f)$. Being in this form, it may be tempting to sample $h_p(t)$ and assign to samples function random variable properties. Nevertheless, there is no consensus on the statistical characterization of acoustic communication channels.

The sort-range LOS acoustic propagation can follow a Friis–Beer–Lambert law. In any case, the Tx and Rx patterns are useful. For a Tx near the surface, at depth z_s below the sea surface, the respective pattern is the so-called Lloyd's Mirror Pattern which is a directional radiation pattern resulting from the interference of the direct and image sources. Note that

the formula depends on the product of wavenumber and source depth so that increasing the frequency has the same effect as increasing the source depth.

$$I(\theta) = 4\sin^2(k \cdot z_s \cos(\theta)) \tag{26}$$

with k being the wavenumber of the environment and theta is the angle of a position vector on the acoustic front with respect to the vertical axis.

Another essential parameter in acoustic propagation models is sound noise. Noise can be ambient noise or site-specific noise. Ambient noise is whatever, not-intended (turbulence, waves, rain, and distant shipping) signal is present in the background of the quiet deep sea. Usually ambient noise, although not white, if often modeled as Gaussian while site-specific, one contains significant non-Gaussian components [48].

2.1.7. Design Considerations for SWSNs

The design of submerged wireless sensor networks operating under electromagnetic and magnetic-induction-based communication paradigms is governed by a set of medium-specific and system-level constraints. Among the most critical factors is the type of water environment, as freshwater and seawater differ substantially in electrical conductivity, which directly determines electromagnetic attenuation and the penetration depth. Higher salinity leads to increased conductive losses, severely limiting the feasible communication range of radiative EM links.

The deployment depth also plays a significant role, as it influences pressure, temperature, and, indirectly, the electrical properties of the medium. While submerged environments are generally more homogeneous than underground scenarios, depth-dependent variations can still affect the attenuation characteristics and coupling efficiency, particularly for near-field magnetic induction links.

Node mobility, caused by water currents or tidal motion, introduces time varying coupling conditions and alignment changes between transmitting and receiving elements. Although Doppler effects are negligible for quasi static MI links and low-frequency EM operation, mobility can still impact link stability and must be considered in system-level design.

Finally, network synchronization and protocol design must account for the short-range, high-attenuation, and energy-constrained nature of submerged EM and MI links. Medium access control and routing strategies should be optimized for reliable short-range communication with predictable channel behavior rather than long-range connectivity.

Overall, submerged wireless sensor networks within the electromagnetic and magnetic induction framework are best suited for short-range, low-power, and high-reliability applications. Accurate propagation modeling, combined with the careful selection of operating frequency, antenna or coil configuration, and deployment geometry, is essential for effective SWSN design and performance evaluation.

2.2. Body Area Networks (BANs)

Body area networks (BANs), (see Figure 7), are specialized wireless networks composed of sensor nodes deployed on, around, or within the human body. These networks support a wide range of medical and health-related applications, including continuous physiological monitoring, implantable medical devices, prosthetic control, and assisted rehabilitation systems. Depending on the relative placement of the communicating nodes, BANs are commonly categorized into on-body, off-body, and in-body communication scenarios, each characterized by distinct propagation mechanisms and design constraints.

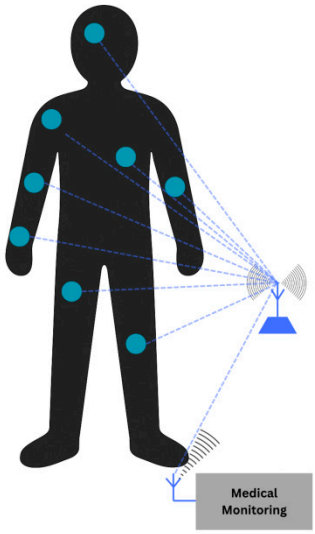

Figure 7. Body WSN.

2.2.1. In-Body Communication

Wireless communication within the human body presents significant challenges due to the complex, heterogeneous, and lossy nature of biological tissues. Human tissues exhibit strong frequency-dependent electromagnetic behavior, with substantial variations in permittivity and conductivity across different tissue types. As a result, signal propagation inside the body is dominated by absorption losses, impedance mismatches at tissue boundaries, and near-field coupling effects rather than conventional free-space radiation.

In addition to propagation efficiency, in-body wireless communication must comply with strict safety constraints related to the specific absorption rate (SAR). Key considerations for limiting SAR include operating at lower-frequency bands to reduce tissue absorption, minimizing transmit power through adaptive power control, optimizing antenna or coil geometry to reduce local field concentration, and selecting modulation schemes that limit peak-to-average power ratios. These considerations are critical to ensuring compliance with international safety guidelines while maintaining reliable in-body communication.

In-body propagation is strongly influenced by the tissue composition and anatomical structure. Organs such as muscle, fat, bone, and blood possess markedly different dielectric properties, leading to spatially varying attenuation and reflection phenomena. Tissues with a high water content, in particular, introduce increased conductive losses, which become especially pronounced at microwave and millimeter-wave frequencies. Furthermore, physiological motion, including respiration and cardiac activity, induces time-varying channel conditions that can affect link stability and reliability over short time scales.

These characteristics necessitate dedicated in-body propagation models and careful selection of the operating frequency, antenna or coil topology, and communication range to ensure the safe and reliable operation of implantable and ingestible wireless devices.

According to IEEE 802.15.6 (https://standards.ieee.org/ieee/802.15.6/5364/, accessed on 23 October 2025) specifications, homogeneous and heterogeneous tissue models are typically evaluated in the 402–405 MHz MICS band and the 2.36–2.4 GHz ISM band. Implanted communication models exhibit significantly higher attenuation due to absorption and impedance mismatches within biological tissues, resulting in predominantly near-field and absorption-dominated propagation. In contrast, non-implanted and on-body models operate under mixed near-field and radiative conditions, with increased susceptibility to surface waves, diffraction, and body-shadowing effects. These differences necessitate distinct modeling assumptions and system design strategies for implanted versus non-implanted scenarios.

Propagation Models and Key Contributions

Numerous studies have modeled the behavior of electromagnetic waves in the human body across various frequency bands, typically focusing on sub-GHz, ISM (2.4 GHz), and UWB ranges.

Dielectric Tissue Modeling (Gabriel Model): Gabriel et al. [49] established a comprehensive dielectric characterization of biological tissues by deriving frequency-dependent Cole–Cole parameters for more than 45 tissue types over the range 10 Hz to 100 GHz. Their study demonstrated extremely wide variability in tissue electromagnetic properties, with relative permittivity values ranging from approximately $\varepsilon_r \approx 1.2 \times 10^6$ for adipose tissue at low frequencies to $\varepsilon_r \approx 4.7$ for cortical bone at millimeter-wave frequencies, while electrical conductivity spans from $\sigma \approx 0.02$ S/m for bone marrow to $\sigma \approx 1.6$ S/m for cerebrospinal fluid. The observed behavior is governed by four major dispersion regions (α, β, γ, and δ), each associated with distinct polarization mechanisms and characteristic relaxation times.

The dielectric response of biological tissues is modeled using multi-dispersion Cole–Cole formulations for the complex permittivity. The simplest representation is the single-pole Debye model, expressed as follows:

$$\hat{\varepsilon} = \varepsilon_\infty + \frac{\varepsilon_s - \varepsilon_\infty}{1 + j\omega\tau}, \tag{27}$$

where $\hat{\varepsilon}$ denotes the complex permittivity, ε_s is the static permittivity, ε_∞ is the permittivity at infinite frequency, ω is the angular frequency, and τ is the relaxation time.

To accurately capture the broadband behavior of real tissues, Gabriel et al. [49] employed a generalized multi-term Cole–Cole model that accounts for multiple dispersion processes and ionic conduction effects:

$$\hat{\varepsilon}(\omega) = \varepsilon_\infty + \sum_n \frac{\Delta\varepsilon_n}{1 + (j\omega\tau_n)^{(1-\alpha_n)}} + \frac{\sigma_i}{j\omega\varepsilon_0}, \tag{28}$$

where $\Delta\varepsilon_n$ represents the strength of the n-th dispersion mechanism, τ_n is the corresponding relaxation time, α_n is the dispersion broadening parameter ($0 \leq \alpha_n \leq 1$), σ_i denotes the ionic conductivity, and ε_0 is the permittivity of free space.

In this formulation, each dispersion term represents a distinct physical polarization mechanism within biological tissues. Specifically, the α-dispersion is associated with ionic diffusion processes at low frequencies, the β-dispersion is primarily linked to polarization at cell membranes and tissue interfaces, and the γ-dispersion corresponds to the relaxation of water molecules at microwave frequencies. These dispersion mechanisms collectively capture the frequency-dependent dielectric behavior of heterogeneous biological tissues and are critical for accurately modeling in-body electromagnetic propagation.

These models achieve deviations below 5% with respect to experimental measurements across the investigated frequency range and remain the reference standard for electromagnetic dosimetry, specific absorption rate (SAR) evaluations, and the design and analysis of implantable and in-body wireless communication systems.

In-Body Propagation at 2.4 GHz ISM Band: Chavez-Santiago et al. [50] performed extensive experimental investigations using anatomical phantoms to characterize electromagnetic propagation within the human body at the 2.4 GHz ISM band. Their measurements revealed path-loss gradients ranging from 1.8 to 2.3 dB/cm in muscle-equivalent tissue, additional attenuation of approximately 12 to 18 dB when the propagation path traverses cortical bone, and polarization-dependent scattering effects resulting in signal variations of up to 6.5 dB. These observations confirm the strongly lossy and heterogeneous nature of in-body propagation at microwave frequencies.

For purely in-body links, the measured path loss was accurately modeled as a linear function of the propagation distance:

$$PL(d) = PL_0 + \alpha\, d, \tag{29}$$

where $PL(d)$ is the path loss in decibels at depth d, PL_0 denotes the reference path loss at a chosen depth origin, and α is the effective attenuation coefficient expressed in dB/cm. This formulation reflects the dominance of absorption losses and near-field coupling effects within biological tissue.

For in-body to off-body communication scenarios, where the signal transitions from the lossy tissue environment to free space, a log-distance path-loss model was adopted for the external propagation segment:

$$PL(d_{\text{in}}, d_{\text{off}}) = PL_0(d_{\text{in}}) + 10\,\gamma(d_{\text{in}})\,\log_{10}\left(\frac{d_{\text{off}}}{d_{\text{ref}}}\right), \tag{30}$$

In this expression, d_{in} represents the implant depth, d_{off} is the external transmitter–receiver separation, d_{ref} is a reference distance in free space, and $\gamma(d_{\text{in}})$ is a depth-dependent path-loss exponent that captures the coupling efficiency between the in-body source and the external environment.

The proposed models were validated against porcine tissue measurements, achieving a coefficient of determination of $R^2 = 0.94$. Compared to legacy free-space or homogeneous-tissue approximations, the models provided approximately 23 percent improvement in the path-loss prediction accuracy for implant depths up to 8 cm, enabling more reliable link budgeting and transmit-power optimization for medical body area networks.

IEEE 802.15.6 Implant Channel Standardization: Chavez-Santiago et al. [51] established the foundational propagation and channel models adopted by the IEEE 802.15.6 standard for medical body area networks. Their work focused on implant communication scenarios in the 2.36 to 2.5 GHz frequency band and provided experimentally validated models for path loss, multipath dispersion, and mobility-induced channel variations.

For in-body to on-body communication links, the measured path-loss exponent was found to vary between $n = 4.1$ and $n = 5.3$, reflecting the strongly lossy and heterogeneous nature of human tissues. Dynamic multipath behavior was observed, with root-mean-square delay spreads ranging from 3.7 ns to 8.2 ns in cardiac implant scenarios. In addition, physiological motion during normal activity introduced Doppler spreads of up to 54 Hz, indicating the moderate time variability of the implant channel. The large-scale path loss is modeled using a log-normal formulation:

$$L(d) = L_0 + 10\, n\, \log_{10}\left(\frac{d}{d_0}\right) + X_\sigma, \tag{31}$$

where $L(d)$ is the path loss in decibels at distance d, L_0 is the reference path loss at distance d_0, n is the path-loss exponent, and X_σ is a zero-mean Gaussian random variable with standard deviation σ, representing log-normal shadowing.

Small-scale multipath effects are described using a tapped-delay-line representation of the channel impulse response:

$$h(\tau) = \sum_{k=1}^{N} a_k\, \delta(\tau - \tau_k), \tag{32}$$

where a_k and τ_k denote the amplitude and delay of the k-th multipath component, respectively. The tap amplitudes are modeled as follows:

$$a_k = \beta_k\, \sqrt{p_k}, \tag{33}$$

with statistical mean power decay given by

$$\mu_k(d) = \Omega_0(d)\, e^{-(k-1)\Lambda(d)}, \tag{34}$$

and depth-dependent standard deviation expressed as

$$\sigma_k(d) = \omega_0(d)\, e^{-(k-1)\lambda(d)}, \tag{35}$$

In these expressions, $\Omega_0(d)$ and $\omega_0(d)$ represent distance-dependent scaling parameters, while $\Lambda(d)$ and $\lambda(d)$ control the exponential decay of the mean and variance of successive multipath components.

The resulting models, formally adopted in the IEEE 802.15.6 standard, indicate signal attenuation gradients of approximately 0.9 to 1.5 dB/cm across twelve representative tissue types. These characteristics enable reliable implant communication for depths up to 5 cm, provided that appropriate power control and modulation strategies are employed.

Ultra-Wideband (UWB) Propagation: Fort et al. [52] experimentally characterized UWB in-body propagation over the 3.1 to 10.6 GHz frequency range using tissue-equivalent phantoms. Their measurements reported a mean root-mean-square delay spread of approximately 4.3 ns in muscle tissue, as well as pronounced frequency-dependent attenuation effects. Comparative analysis across frequency bands revealed 18 to 24 dB lower path loss in sub-1 GHz bands relative to higher microwave frequencies for identical implant depths. In addition, pulse distortion measurements indicated waveform preservation below 7 percent at an implantation depth of 15 cm, highlighting the severe dispersive nature of in-body channels at UWB frequencies.

The large-scale path loss was modeled using a classical log-distance formulation:

$$PL(d) = PL_0 + 10\, n \log_{10}\left(\frac{d}{d_0}\right), \tag{36}$$

where $PL(d)$ denotes the path loss in decibels at depth d, PL_0 is the reference path loss at distance d_0, and n is the path-loss exponent capturing frequency- and tissue-dependent attenuation.

Phantom measurements further indicated frequency-dependent attenuation gradients ranging from 0.4 to 1.2 dB/cm across the investigated spectrum. These results support the conclusion that, despite the high temporal resolution offered by UWB signaling, lower-frequency operation in the 400 to 900 MHz band provides superior penetration efficiency for deep implant communications, achieving up to 92 percent power efficiency compared to UWB operation at greater depths.

In Vivo Channel Characterization: Demir et al. [53] proposed a hybrid framework that combines in vivo measurements, numerical modeling, and data-driven correction to characterize electromagnetic propagation in body area networks. Their study included 3.5 GHz in vivo measurements across twelve anatomical sites using porcine models, achieving a root-mean-square error of 2.4 dB. Dynamic specific absorption rate (SAR) mapping revealed variations below 0.8 W/kg over respiratory cycles, while the machine-learning-assisted correction of multilayer FDTD simulations improved agreement with live-tissue measurements to 91 percent accuracy.

Within this framework, a progression of propagation models was employed, ranging from baseline free-space formulations to enhanced models accounting for antenna mismatch, boundary reflections, and tissue absorption, as well as statistical path-loss representations.

Basic free space path loss (FSPL)

$$P_r = P_t\, G_t\, G_r \left(\frac{\lambda}{4\pi R}\right)^2, \tag{37}$$

where P_t and P_r denote the transmitted and received powers, G_t and G_r are the transmitter and receiver antenna gains, λ is the wavelength, and R is the separation distance.

FSPL with reflection and mismatch losses

$$P_r = P_t\, G_t \left(1- \mid S_{11} \mid^2\right) G_r \left(1- \mid S_{22} \mid^2\right) \left(\frac{\lambda}{4\pi R}\right)^2, \tag{38}$$

where S_{11} and S_{22} are the input reflection coefficients at the transmitter and receiver, respectively. The terms $\left(1- \mid S_{11} \mid^2\right)$ and $\left(1- \mid S_{22} \mid^2\right)$ represent power accepted by the antennas due to impedance matching. FSPL with reflection loss and tissue absorption

$$P_r = P_t\, G_t \left(1- \mid S_{11} \mid^2\right) G_r \left(1- \mid S_{22} \mid^2\right) \left(\frac{\lambda}{4\pi R}\right)^2 e^{-2\alpha R}, \tag{39}$$

where α is the medium attenuation constant in nepers per meter. The exponential term models power decay due to absorption within biological tissue.

Statistical path-loss model

$$PL(d) = PL(d_0) + 10\, n \log_{10}\left(\frac{d}{d_0}\right) + X_\sigma, \tag{40}$$

where $PL(d)$ is the path loss in decibels at distance d, $PL(d_0)$ is the reference path loss at distance d_0, n is the path-loss exponent, and X_σ is a zero-mean Gaussian random variable accounting for log-normal shadowing.

Using this hierarchical modeling approach, Demir et al. [53] demonstrated that conventional homogeneous phantoms underestimate losses at bone interfaces by approximately 18 to 22 percent, underscoring the importance of multilayer anatomical modeling and adaptive correction when designing reliable BAN communication links.

Flexible Implantable Antenna Design: Zahid et al. [54] presented a flexible and biocompatible implantable antenna operating at 2.4 GHz, specifically designed for in-body body area network applications. The proposed antenna employed a meandered dipole topology fabricated on a liquid crystal polymer (LCP) substrate with relative permittivity $\varepsilon_r = 3.2$, enabling mechanical flexibility and stable electromagnetic performance in biological environments.

Experimental and numerical evaluations in tissue-equivalent phantoms demonstrated a realized gain of up to 8.2 dBi, with performance variations below 1.5 dB across different tissue types. The antenna achieved a radiation efficiency of approximately 94 percent in muscle-equivalent media, while maintaining compliance with specific absorption-rate constraints, with peak SAR values below 1.6 W/kg under standard operating conditions. Owing to its compact meandered configuration, the design occupied a footprint approximately 23 percent smaller than that of conventional implantable antennas operating at the same frequency.

Link-level performance analysis indicated achievable data rates of up to 47 Mbps at an implantation depth of 12 mm. In heterogeneous tissue simulations, the proposed antenna-based communication system outperformed comparable magnetic induction-based solutions by approximately 18 percent in terms of link efficiency, highlighting the potential of optimized radiative antenna designs for short-range, high-data-rate implantable applications.

Hybrid In-Body to On-Body Propagation: Liu et al. [55] investigated hybrid in-body to on-body electromagnetic propagation for ultra-wideband (UWB) systems operating over the 3.1 to 10.6 GHz frequency range. Extensive simulations and measurements across twelve anatomical sites revealed path-loss gradients between 2.1 and 3.8 dB/cm in muscle tissue, pronounced polarization dependence with 40 to 65 percent lower attenuation for transverse polarization compared to longitudinal orientation, and deviations below 4.5 dB between heterogeneous human models and tissue-equivalent phantom measurements at an implantation depth of 4 cm. These results confirm the strong influence of the tissue composition and polarization on hybrid in-body to on-body links.

The dielectric properties of biological tissues were modeled using a four-pole Cole–Cole formulation, enabling the accurate representation of broadband dispersive behavior:

$$\hat{\varepsilon}_r(\omega) = \varepsilon_\infty + \sum_{n=1}^{4} \frac{\Delta\varepsilon_n}{1 + (j\omega\tau_n)^{1-\alpha_n}} + \frac{\sigma_0}{j\omega\varepsilon_0}, \tag{41}$$

where $\hat{\varepsilon}_r(\omega)$ denotes the complex relative permittivity, ε_∞ is the permittivity at high frequencies, $\Delta\varepsilon_n$ and τ_n represent the strength and relaxation time of the n-th dispersion mechanism, α_n is the Cole–Cole broadening parameter, σ_0 is the effective ionic conductivity, and ε_0 is the permittivity of free space.

To capture transitions between propagation regimes, the authors employed a piecewise path-loss formulation incorporating a distance-dependent breakpoint:

$$PL(d) = PL_0 + 10\, n \log_{10}\left(\frac{d}{d_0}\right) + a\,(d - d_b)\,\mathbb{I}(d > d_b) + X_\sigma, \tag{42}$$

where PL_0 is the reference path loss at distance d_0, n is the path-loss exponent, a is an additional linear attenuation coefficient beyond the breakpoint distance d_b, $\mathbb{I}(\cdot)$ is the indicator function, and X_σ represents log-normal shadowing.

The channel transfer function and corresponding impulse response were obtained directly from measured voltage waveforms as follows:

$$H(f) = \frac{\mathcal{F}\{U_r(t)\}}{\mathcal{F}\{U_t(t)\}}, \tag{43}$$

$$h(t) = \mathcal{F}^{-1}\{H(f)\} = \mathcal{F}^{-1}\left\{\frac{\mathcal{F}\{U_r(t)\}}{\mathcal{F}\{U_t(t)\}}\right\}, \tag{44}$$

where $U_t(t)$ and $U_r(t)$ denote the transmitted and received voltage signals in the time domain, respectively. The resulting multilayer anatomical model achieved a prediction accuracy of 92.3 percent for signal leakage patterns under dynamic organ motion, highlighting the importance of anatomically realistic and dispersive tissue modeling.

Conductive Body Channel Communication: Ferguson and Redish [56] investigated conductive body channel communication as a quasi-static electromagnetic alternative for short-range in-body links. Their approach exploited tissue conductivity at carrier frequencies between 40 and 200 kHz, achieving data transmission energies below 1 nJ/bit. Experimental results demonstrated path-loss reductions of 3.2 to 8.7 dB compared to conventional RF-based implant links, while adaptive impedance matching reduced reflection losses by 12 to 18 dB. Using galvanic coupling, packet reception rates of up to 98.7 percent were achieved at implantation depths of 5 cm.

In addition to improved link efficiency, conductive coupling exhibited significantly reduced electromagnetic exposure, yielding an approximately 60 percent lower specific absorption rate compared to radiative implant communication in neural stimulation scenarios. These results establish conductive body channel communication as a viable complemen-

tary solution for ultra-low-power, short-range implantable systems operating within strict SAR constraints.

Wireless communication inside the human body presents significant challenges due to the complex, heterogeneous, and lossy nature of biological tissues. Human organs and tissues exhibit pronounced variability in dielectric permittivity and electrical conductivity, which leads to strong frequency-dependent attenuation, impedance mismatches at tissue boundaries, and nonuniform propagation paths. As a result, in-body electromagnetic propagation deviates significantly from free-space behavior and is dominated by absorption losses and near-field coupling effects rather than conventional radiative mechanisms.

Tissue composition is a dominant factor in shaping channel characteristics, as structures such as fat, muscle, bone, and blood possess markedly different electromagnetic properties. Tissues with a high water content, in particular, introduce increased conductive losses, which become increasingly severe at microwave and millimeter-wave frequencies. In addition, reflections and scattering at interfaces between adjacent tissue layers further contribute to signal degradation and spatial variability of the channel.

Beyond static anatomical effects, the in-body communication environment is inherently dynamic. Physiological motion, including respiration, cardiac activity, and organ displacement, induces time-varying channel conditions that can affect link stability, polarization alignment, and received signal strength. These combined effects necessitate dedicated propagation models and adaptive system designs to ensure reliable and safe operation of in-body wireless links.

Practical Considerations in In-Body Networks

The design and modeling of in-body wireless networks are constrained by a combination of electromagnetic, biological, and regulatory factors. Operating frequency selection represents a primary trade-off, as lower frequencies offer improved penetration through biological tissues but require physically larger radiating or coupling structures. Conversely, operation at higher frequencies enables compact antenna designs at the expense of increased absorption losses and reduced effective communication range.

Implantable devices are inherently energy-constrained and must operate under strict power and specific absorption rate (SAR) limits, necessitating highly efficient transmission schemes and adaptive power control. Material biocompatibility further constrains the antenna and packaging design, as substrates, conductors, and encapsulation layers must ensure long-term stability without adverse interaction with surrounding tissues. Finally, clinical deployment requires compliance with established regulatory frameworks, including IEEE 802.15.6 specifications and medical device safety standards, which directly influence allowable frequency bands, radiated power levels, and the system architecture.

Despite ongoing advances, in-body wireless communication remains among the most technically demanding body-centric scenarios due to severe propagation losses, tissue heterogeneity, and time-varying anatomical conditions. Continued progress in electromagnetic modeling, hybrid coupling techniques, and simulation-driven validation is therefore essential for reliable and safe implantable communication systems.

2.2.2. On-Body and Off-Body Communication

On-body and off-body communication scenarios address electromagnetic propagation along the body surface and between the human body and external infrastructure, respectively. Unlike in-body links, these channels are dominated by surface waves, creeping waves, diffraction around anatomical structures, and intermittent line-of-sight (LOS) conditions. Such links form the backbone of wearable health monitoring systems, medical telemetry, and body-centric sensing networks.

Channel Characteristics and Modeling Challenges

On-body and off-body propagation is strongly influenced by continuous human motion, which introduces time-varying shadowing, polarization mismatch, and Doppler components. Body curvature and posture determine the availability of direct and diffracted propagation paths, while the antenna placement and orientation govern coupling efficiency to surface and creeping waves. In addition, interactions with clothing, accessories, and skin properties further modify the effective propagation environment, resulting in statistically nonstationary channel behavior.

Key Contributions

WBAN Propagation Fundamentals: Movassaghi et al. [57] synthesized over 120 experimental and analytical studies to establish a unified framework for wireless body area network propagation. Their analysis quantified path-loss variations of 14 to 28 dB due to body curvature, polarization mismatch penalties of 5 to 11 dB in dynamic scenarios, and creeping-wave attenuation rates between 0.8 and 1.4 dB/cm at 2.4 GHz. Safety considerations were evaluated through the specific absorption rate, defined as

$$\mathrm{SAR} = \frac{\sigma \mid E \mid^2}{\rho}, \tag{45}$$

where σ is the tissue conductivity, E is the root-mean-square electric field strength, and ρ is the tissue mass density. Their survey identified ultra-wideband operation as particularly resilient to motion-induced shadowing, with the majority of reported studies exhibiting less than 3 dB signal fluctuation during walking speeds of 1 to 1.5 m/s.

Energy-Aware Routing Under Channel Variations: Behera et al. [58] analyzed cross-layer routing strategies under fading conditions, demonstrating significant energy savings through mobility-aware and location-adaptive protocols. Cluster-head selection was governed by an energy-aware threshold function

$$T(n) = \frac{P}{1 - P\left(r \mathrm{m} \frac{1}{P}\right)} \cdot \frac{E_{\mathrm{current}}}{E_{\max}}, \tag{46}$$

where P is the desired cluster-head probability, r is the current round, E_{current} is the residual node energy, and $E_{\max}$ is the initial energy. The total network energy consumption was modeled as

$$E_{\mathrm{tot}} = N_{\mathrm{rnd}}\, E_{\mathrm{TX}}\, q + 5\, E_{\mathrm{ADRSE}}, \tag{47}$$

with the aggregated data reception and transmission energy expressed as

$$E_{\mathrm{ADRSE}} = E_{\mathrm{RX,elec}}\, q\left(\frac{N}{k} - 1\right) + \frac{N}{k}\, q\left(E_{\mathrm{TX,elec}} + \varepsilon_{\mathrm{amp}} d^m\right), \tag{48}$$

Polarization and Antenna Configuration: Cotton and Scanlon [59] investigated polarization-dependent fading in body-centric channels using advanced statistical models. Signal envelopes were shown to follow Weibull statistics

$$p_R(r) = \frac{\beta}{\lambda} r^{\beta-1} e^{-\frac{r^\beta}{\lambda}}, \tag{49}$$

and, under dominant line-of-sight conditions, the more general κ–μ distribution

$$f(\rho) = \frac{2\mu\left(1+\kappa\right)^{\frac{\mu+1}{2}}}{\kappa^{\frac{\mu-1}{2}} e^{\mu\kappa}} \rho^\mu e^{-\mu(1+\kappa)\rho^2} I_{\mu-1}\left(2\mu\sqrt{\kappa(1+\kappa)}\,\rho\right), \tag{50}$$

Temporal fading behavior was quantified through the level crossing rate

$$N_R(r) = \sqrt{2\pi}\, f_m \, \frac{\mu^{\frac{1}{2}}(1+\kappa)^{\frac{\mu}{2}}}{\kappa^{\frac{\mu-1}{2}} e^{\mu\kappa}} \rho^{\mu} e^{-\mu(1+\kappa)\rho^2} I_{\mu-1}\left(2\mu\sqrt{\kappa(1+\kappa)}\,\rho\right), \tag{51}$$

Diversity combining was analyzed using maximal ratio combining

$$R = \sqrt{r_1^2 + r_2^2 + \cdots + r_M^2}, \tag{52}$$

and equal gain combining

$$R = \frac{r_1 + r_2 + \cdots + r_M}{\sqrt{M}}, \tag{53}$$

Their work quantified how the antenna configuration and body movement affect these statistical parameters, providing crucial design insights for reliable body-centric links.

Dynamic On-Body Channel Characterization: Cheffena [60] developed a time-variant on-body channel model incorporating human gait kinematics. Walking dynamics were related to cycle parameters through

$$v_r = lf, l = 1.346\sqrt{v_r}, \tag{54}$$

Antenna displacement and rotation were modeled empirically, yielding time-varying antenna gain

$$G_{t'}(\theta, \phi) = G\left(\theta + \Delta\theta_{t'}, \phi + \Delta\phi_{t'}\right), \tag{55}$$

Diffraction effects were characterized using Fresnel zone analysis

$$R_1 = \sqrt{\frac{\lambda ab}{a+b}}, \tag{56}$$

The model combined deterministic limb movement patterns with stochastic fading components, achieving 88% accuracy in predicting signal drops during rapid posture changes.

Millimeter-Wave Off-Body Propagation: Pellegrini et al. [61,62] analyzed 60 GHz body-centric channels using the free-space reference model

$$PL_{\mathrm{FS}}(d) = 20\log_{10}\left(\frac{4\pi d}{\lambda}\right), \tag{57}$$

and quantified additional losses introduced by body shadowing and polarization mismatch. Their meta-analysis established practical antenna design guidelines for wearable millimeter-wave systems.

Standardized On/Off-Body Testing: Shon et al. [63,64] demonstrated a wireless neural interface operating over 3.2 to 4.5 GHz UWB, achieving reliable data transmission with minimal sensitivity to limb motion. Neural stimulation currents were governed by Ohm's law

$$I_{\mathrm{stim}} = \frac{V_{\mathrm{stim}}}{R_{\mathrm{stim}}}, \tag{58}$$

ensuring precise and safe control of tissue excitation levels.

Practical Considerations

The design of on-body and off-body wireless body area networks is strongly influenced by antenna characteristics, energy constraints, and the surrounding electromagnetic environment. Wearable antenna implementations must accommodate body curvature and motion while maintaining stable impedance matching and radiation characteristics.

Flexible and skin-conformal antenna designs have been shown to reduce mismatch losses and improve link reliability, particularly under dynamic conditions, while also enhancing user comfort and long-term wearability.

Energy efficiency remains a critical design constraint for on-body sensor nodes, which typically operate on limited battery capacity or energy-harvesting sources. Communication strategies must therefore balance the transmit power, data rate, and robustness against channel variability to prolong the operational lifetime without compromising link reliability.

In addition, body area networks must operate in increasingly congested spectral environments. Coexistence with other wireless technologies, including Wi-Fi, Bluetooth, and cellular systems, introduces interference that can degrade performance if not properly accounted for. Robust channel modeling and adaptive communication strategies are essential to mitigate interference effects and ensure reliable operation in real-world deployment scenarios.

Overall, the breadth of existing experimental and modeling studies demonstrates that reliable on-body and off-body communication requires propagation models capable of adapting to human mobility, complex body geometries, and time-varying environmental conditions. Future research directions are expected to emphasize data-driven and adaptive electromagnetic channel modeling techniques, as well as cross-layer design approaches that jointly optimize antenna behavior, propagation modeling, and network protocols for body-centric wireless systems.

It is noted that the SAR distribution varies significantly across different regions of the human body. Due to anatomical and dielectric differences, SAR levels are typically higher in the head and trunk regions, where the tissue density and water content are greater, compared to the limbs. Antenna placement, orientation, and proximity to sensitive organs therefore play a critical role in on-body and off-body system design, and a region-specific SAR evaluation is essential for ensuring safe operation.

2.3. Indoor and Outdoor Wireless Sensor Networks (WSNs)

Wireless sensor networks deployed in indoor and outdoor environments support a wide range of applications, including smart buildings, environmental monitoring, industrial automation, and security systems. Unlike underground, submerged, or body-centric scenarios, indoor and outdoor WSNs typically operate in air but are strongly influenced by the environmental geometry, material composition, and human activity. These factors introduce propagation phenomena that require environment-specific modeling approaches.

2.3.1. Indoor Wireless Sensor Networks

Indoor environments represent one of the most complex propagation scenarios for wireless sensor networks due to rich multipath conditions, signal attenuation through structural elements, and coexistence with numerous wireless systems. Channel behavior is highly dependent on the building layout, construction materials, and dynamic human presence, resulting in strong spatial and temporal variability.

Key Channel Modeling Considerations

Indoor wireless propagation is dominated by multipath and reflection mechanisms, as signals interact with walls, ceilings, floors, furniture, and metallic objects, producing constructive and destructive interference patterns. In addition, wall and floor penetration losses introduce significant attenuation that depends on the material type and thickness. Typical indoor deployments, (see Figure 8), also involve high device density, where WSN nodes must coexist with Wi-Fi, Bluetooth, and other RF systems, leading to increased interference and spectrum contention.

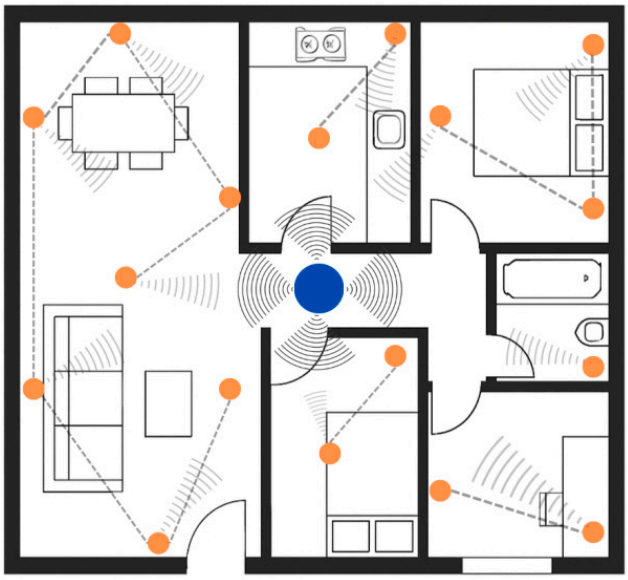

Figure 8. Indoor WSN.

Notable Propagation Models and Contributions

Millimeter-Wave Channel Modeling: Samimi and Rappaport [65] developed a three-dimensional statistical channel model for indoor millimeter-wave propagation, validated at 28 GHz and 73 GHz. Their model characterizes spatial consistency, polarization-dependent path-loss exponents ranging from 2.1 to 3.8, and time-evolving multipath components caused by human blockage and mobility. The geometry-based stochastic framework achieved standard deviation errors below 1.7 dB compared to extensive real-world measurements and has been widely adopted in 5G NR channel modeling.

The large-scale path loss follows a log-distance formulation:

$$PL(d) = PL(d_0) + 10n\log_{10}\left(\frac{d}{d_0}\right) + X_\sigma, \tag{59}$$

where n is the path-loss exponent and X_σ models log-normal shadowing.

Hybrid Data-Driven Modeling: Zakeri et al. [66] proposed a hybrid data-driven framework that combines deep neural networks for multi-material penetration loss estimation with gradient-boosted decision trees for diffraction modeling. Their approach demonstrated improved real-time prediction accuracy over classical ray-tracing, achieving a mean absolute error of 2.3 dB for penetration loss and an R^2 of 0.94 for diffraction gain estimation. This work highlights the potential of learning-based models to complement deterministic techniques in complex indoor environments.

Empirical Models for Specific Environments: Seidel and Rappaport [67] introduced statistical indoor propagation models for office environments, capturing signal behavior in cubicles, corridors, and open-plan spaces. These empirical formulations remain widely used for baseline performance evaluations of indoor wireless systems due to their simplicity and measurement-based grounding.

Floor Attenuation Factor Models: For multi-story buildings, Hashemi [68] proposed the Multi-Floor Propagation Model, which augments the log-distance path-loss expression with a floor attenuation factor:

$$PL(d) = PL(d_0) + 10n\log_{10}\left(\frac{d}{d_0}\right) + \sum_{i=1}^{N_f} FAF_i, \tag{60}$$

where FAF_i represents the attenuation introduced by the i-th intervening floor and N_f is the number of floors between transmitter and receiver.

Ultra-Wideband Indoor Models: Briso et al. [69] conducted extensive ultra-wideband measurements across industrial and office environments, reporting RMS delay spreads between 1.8 and 4.3 ns and frequency-dependent path-loss exponents in the range 1.7 to 2.3. Their multi-slope path-loss model achieved standard deviation errors of approximately 1.9 dB and highlighted the strong sensitivity of UWB channels to line-of-sight conditions.

Measurement-Driven Deep Learning Models: Li et al. [70] introduced TransPathNet, a transformer CNN hybrid framework for indoor radio map construction. By combining coarse-grained path-loss estimation with fine-grained multipath correction, their model achieved a median localization error of 0.8 m, outperforming conventional CNN-based approaches while maintaining scalability across diverse building types.

Body Shadowing and Human Mobility: Patwari and Wilson [71] analyzed the impact of human mobility on indoor signal variability, demonstrating that moving bodies introduce time-varying shadowing and fading effects that significantly affect link reliability. Their findings emphasize the need for channel models that explicitly account for dynamic obstructions in realistic indoor WSN deployments.

Practical Implementation Considerations

The deployment of indoor wireless sensor networks requires the careful consideration of node placement, as strategic positioning can reduce coverage gaps and mitigate severe multipath fading. Adaptive power control mechanisms are essential to balance connectivity and energy efficiency in dense indoor environments. Furthermore, models that incorporate environmental awareness, such as temperature or humidity sensing, can enhance prediction accuracy by adapting propagation parameters to changing indoor conditions.

Overall, the combination of empirical, deterministic, and learning-based models provides a comprehensive toolbox for indoor WSN channel characterization. As smart buildings and large-scale IoT deployments continue to expand, propagation models capable of capturing real-time environmental dynamics and human activity will become increasingly important.

2.3.2. Outdoor Wireless Sensor Networks

Outdoor wireless sensor networks support a broad range of applications, including environmental monitoring, precision agriculture, transportation infrastructure supervision, and urban sensing (see Figure 9). Compared to indoor deployments, outdoor scenarios typically involve larger spatial scales, a variable terrain morphology, and stronger environmental coupling, resulting in propagation characteristics that differ substantially from enclosed environments.

Key Channel Modeling Considerations

Outdoor wireless propagation is strongly affected by terrain and surface features such as vegetation, buildings, hills, and ground irregularities, which introduce diffraction, scattering, and shadowing effects. Vegetation density and seasonal variations further modify channel characteristics by altering moisture content and foliage distribution, leading to time-varying attenuation. In addition, outdoor WSN deployments frequently alternate between line-of-sight and non-line-of-sight conditions, particularly in urban and suburban environments, necessitating models that can accommodate mixed propagation regimes.



Figure 9. Outdoor WSN.

Notable Propagation Models and Contributions

Classical empirical models such as the Okumura–Hata and COST 231-Hata formulations remain widely used for outdoor WSN planning due to their simplicity and measurement-based grounding. The Okumura–Hata model provides median path-loss predictions for suburban and rural environments, while the COST 231-Hata extension incorporates additional parameters to account for urban morphology, including base-station height and building density.

For urban environments, the COST 231-Hata model is commonly expressed as

$$PL(d) = 46.3 + 33.9\log_{10}(f) - 13.82\log_{10}(h_b) - a(h_m) + \left[44.9 - 6.55\log_{10}(h_b)\right]\log_{10}(d) + C \quad (61)$$

where f is the carrier frequency in MHz, h_b and h_m are the base-station and mobile antenna heights, respectively, d is the transmitter–receiver separation in kilometers, $a(h_m)$ is the mobile antenna height correction factor, and C is an environment-dependent constant [72,73].

In the COST 231-Hata formulation, the environmental constant C depends on the deployment scenario and typically takes the value C = 0 dB for suburban and rural environments and C = 3 dB for dense urban environments. These values reflect additional losses due to an increased building density and urban morphology.

Urban vs. Rural Comparative Models: Nassef et al. [74] performed a comparative analysis of outdoor WSN performance across seventeen deployment sites, demonstrating that rural environments can exhibit up to 23 percent higher median path loss compared to urban areas due to dense vegetation and uneven terrain. Their measurements further showed that large-scale shadowing followed a Weibull distribution with shape parameter k $\approx$ 1.8 in rural scenarios, while urban shadowing was better modeled using log-normal statistics. These findings highlight the importance of environment-specific shadowing models when designing outdoor WSNs.

Two-Ray and Ground-Reflection Models: For open-area deployments with elevated antennas and minimal obstructions, the two-ray ground-reflection model provides a useful approximation of outdoor propagation. In this model, the received power is determined by

the superposition of the direct and ground-reflected rays, leading to a distance-dependent path-loss behavior given by

$$PL(d) \propto \left(\frac{h_t h_r}{d^2}\right)^2, \tag{62}$$

where h_t and h_r denote the transmitter and receiver antenna heights, respectively. This model is particularly relevant for agricultural and highway monitoring applications, where antenna heights and ground properties dominate propagation behavior.

Shadowing, Diffraction, and Dynamic Obstructions: Additional studies have addressed diffraction over rooftops, shadowing behind tall buildings, and the influence of mobile obstructions such as vehicles and pedestrians on link stability. These effects introduce slow and fast fading components that are not captured by purely distance-based models and often require statistical or hybrid deterministic–statistical formulations for accurate characterization.

Practical Implementation Considerations

The deployment of outdoor wireless sensor networks requires careful antenna height selection and node placement to mitigate ground-level obstructions and improve line-of-sight probability. Energy-efficient routing protocols are essential, as outdoor WSNs typically span large geographic areas and rely on multi-hop communication strategies. Furthermore, incorporating environmental adaptivity into propagation models, such as responsiveness to meteorological conditions including rainfall, fog, and wind, can significantly enhance communication reliability and the network lifetime.

Overall, the reviewed propagation models and experimental studies provide a solid theoretical and practical foundation for selecting and adapting outdoor WSN channel models according to deployment environment, terrain characteristics, and operational requirements.

3. Results

This section presents simulation and analytical results for representative wireless sensor network deployment environments and associated propagation models. The objective is to quantify performance trends across soil (underground), submerged, in-body, indoor, and outdoor scenarios under parameter sets summarized in Table 1. For each environment, results are generated using the corresponding physical model and frequency range introduced in Section 2, enabling a consistent comparison of the attenuation behavior and feasibility limits across media. The results are organized by scenario to preserve physical interpretability. The section concludes with feasibility screening and Pareto-type comparisons across communication modalities, highlighting the dominant trade-offs among the energy per bit, achievable range, and data rate.

Table 1. Key simulation characteristics and model equations.

Figures	Scenario	Fundamental Principle	Equation
Figure 10a	Underground RF and MI propagation	Complex permittivity soil model	$PL = 20\cdot\log_{10}(4\pi rf/c) + a_{soil}\cdot r$, $a_{soil} \propto \pi f\mu\sigma$
Figure 10b	Sensitivity analysis of Soil parameters	ΔPL due to change in ε_r, σ	Decimal differentiation in soil mixing prices
Figure 11	Shallow Fresh Water	Exponential attenuation for EM	$PL_{EM} = 20\cdot\log(4\pi rf/c) + water$

Table 1. *Cont.*

Figures	Scenario	Fundamental Principle	Equation
Figure 12a,b	In-body propagation and absorption	Debye/Cole-Cole tissue model and exponential attenuation	$PL = 20 \cdot \log10(4\pi rf/c) + 8.68 \cdot a_{tissued} \cdot d$
Figures 13a,b and 14a,b	Operation at mm-Waves in indoor	Multi-Wall Model and shadowing log-normal	$PL = PL_0 + 10 \cdot n \cdot \log_{10}(r) + \sum L_{wall,i} + X$
Figure 15a,b	Outdoor LOS link at 24 GHz	Friis Free Space and Gaussian calibration Noise	$PL = 20 \cdot \log_{10}(4\pi rf/c) + N(0,cal)$
Figure 16	3GPP UMi LOS/NLOS Model	3GPP TR 38.901	LOS/NLOS mean and σ, weighted by P_LOS(d)
Figure 17	Cross Tech Performance	SNR gated Feasibility and Energy model	$Eb = Pt/Rb,\ LAT = 1/Rb,$ $SNR \geq SNR_{min}$

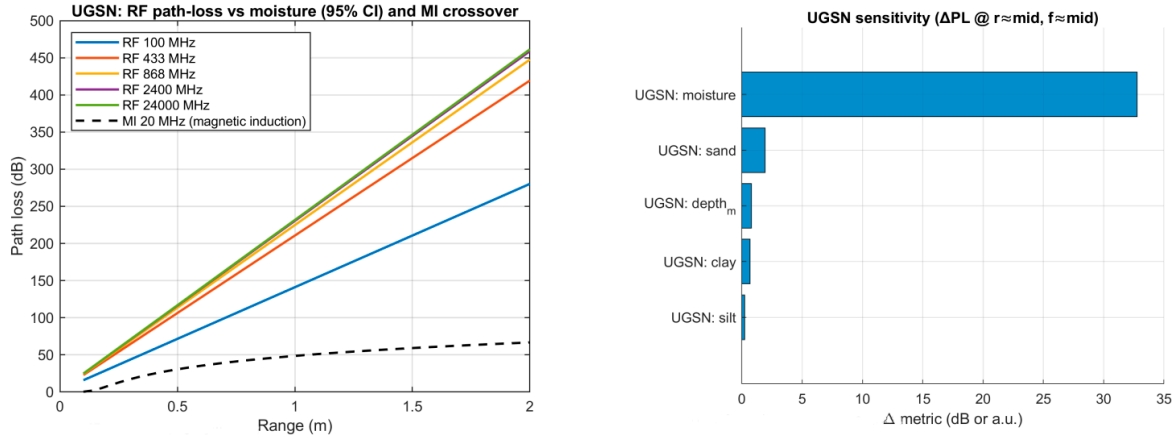

(**a**) (**b**)

Figure 10. (**a**) RF Path-Loss and moisture 95% CI. (**b**) Different soil materials and attenuation.

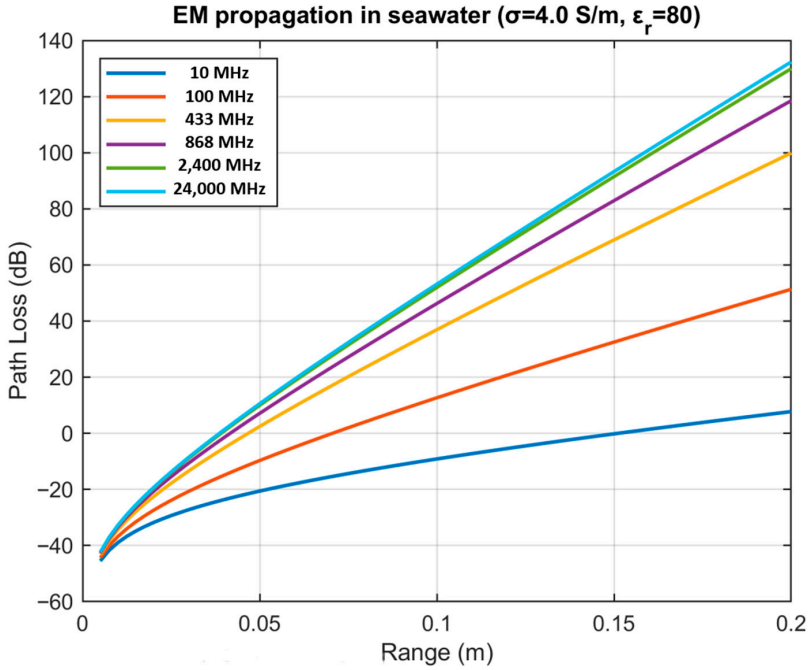

Figure 11. Electromagnetic waves for short range in submerge WSN.

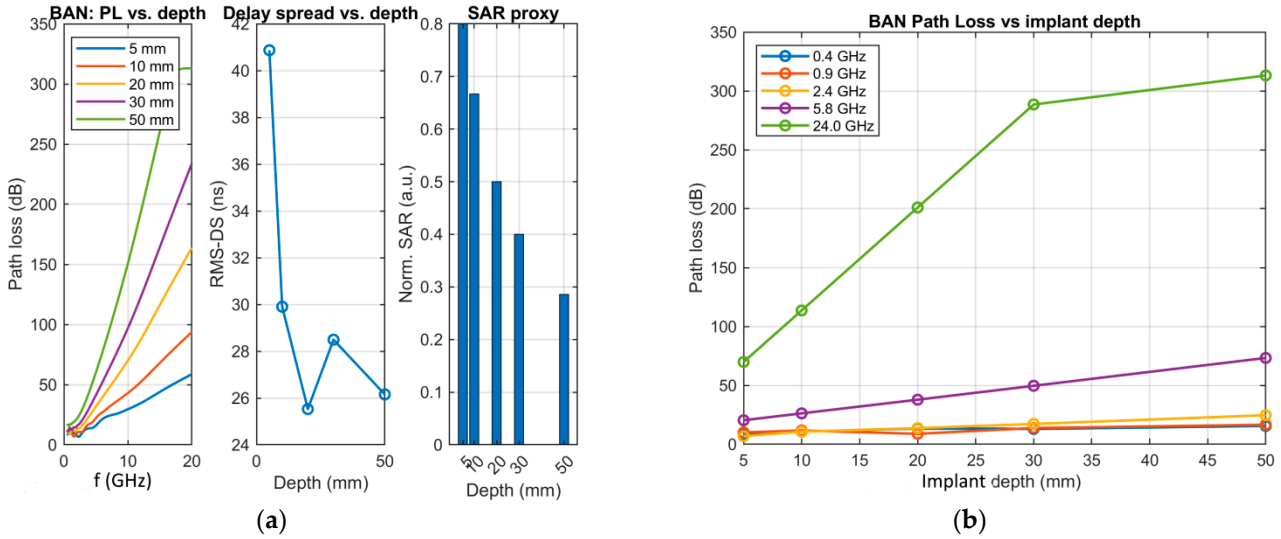

(**a**) (**b**)

Figure 12. (**a**) Metrics for the human body. (**b**) BAN path loss vs. implant depth.

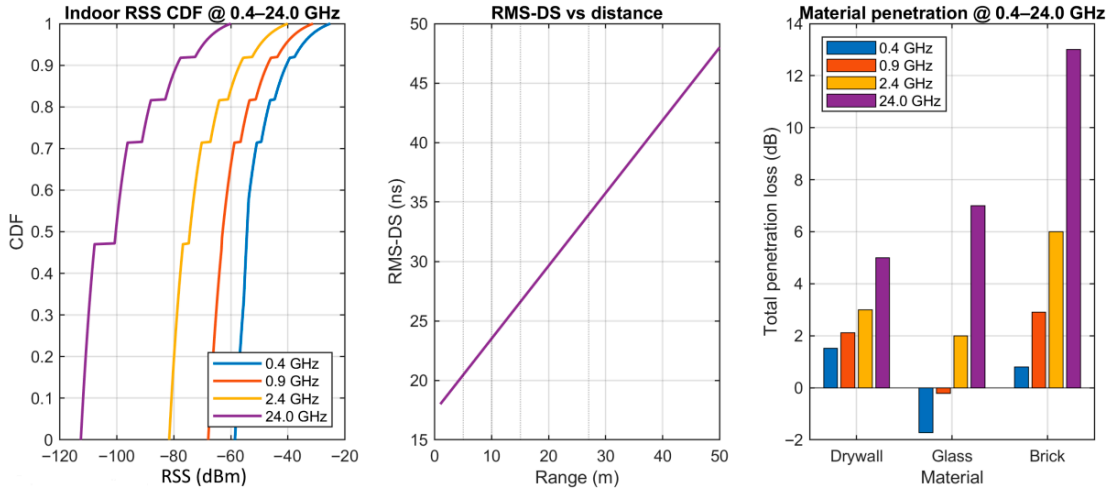

(**a**) (**b**)

Figure 13. (**a**) Metrics for indoor WSN. (**b**) Path loss for multiwall indoor environment at 24 GHz.

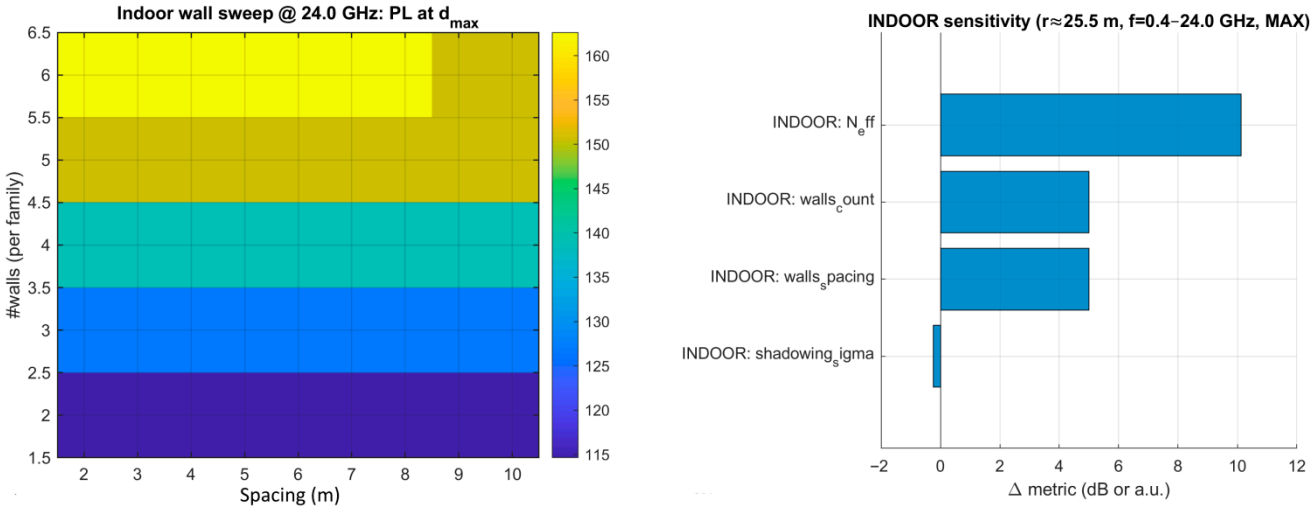

(**a**) (**b**)

Figure 14. (**a**) Indoor wall sweep at 24 GHz PL at d_{max}. (**b**) Indoor sensitivity at 25.5 m and 24 GHz.

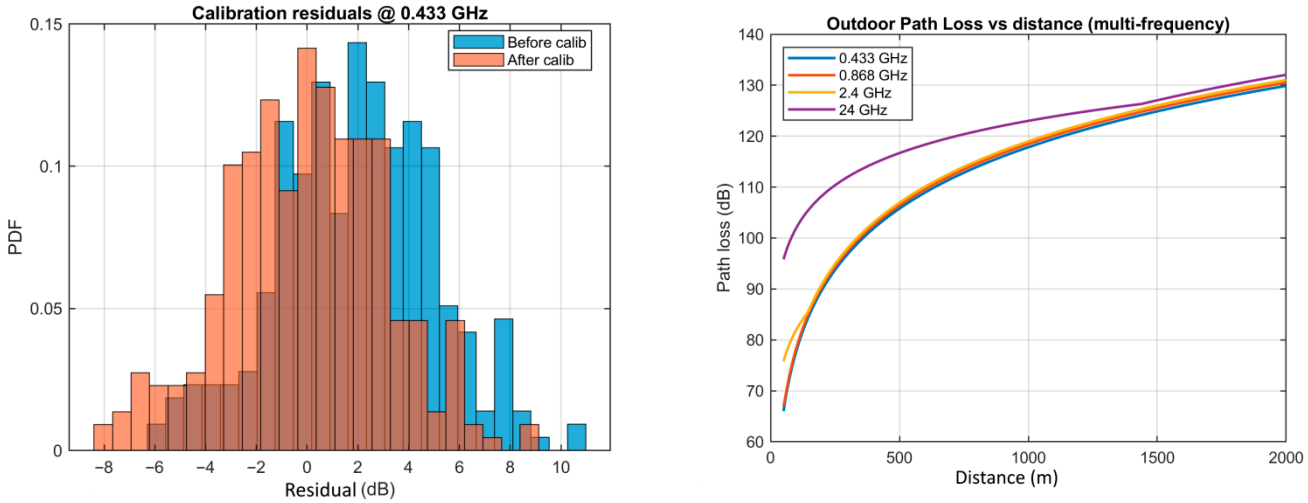

(**a**) (**b**)

Figure 15. (**a**) Outdoor RSS at 24 GHz. (**b**) Outdoor path loss vs. distance at 24 GHz.

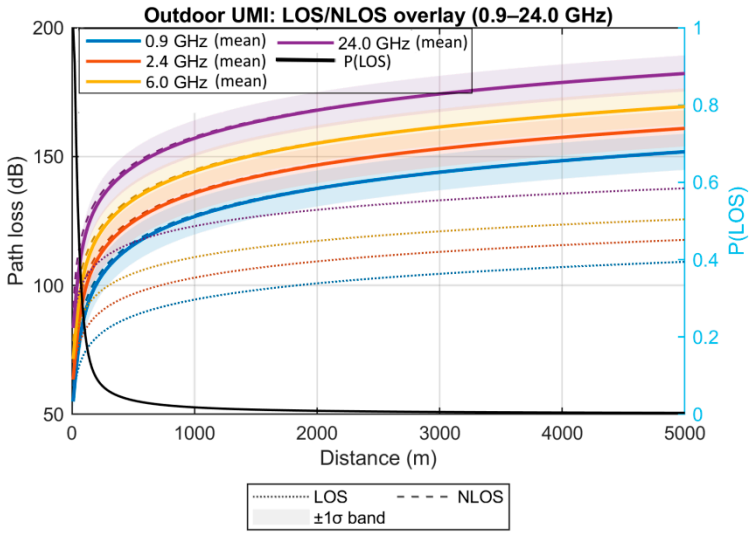

Figure 16. 3GPP UMi path loss model with LOS/NLOS overlay at 24.0 GHz.

3.1. Path Loss and Sensitivity Study in Soil-Based Communication

A graphical representation of the simulated path loss across multiple frequency bands is shown in Figure 10a. Specifically, the figure illustrates path-loss variation for three radio-frequency links operating at 433 MHz, 868 MHz, and 2.4 GHz, together with a magneto-inductive (MI) link operating at 20 MHz. All results correspond to moist soil conditions and are presented with a 95% confidence interval, highlighting the influence of soil conductivity on signal attenuation.

As expected, path loss increases approximately linearly with both the burial depth and horizontal separation, primarily due to absorption and scattering within the lossy soil medium. A distinct crossover point appears at approximately 1 m, beyond which the MI link exhibits lower attenuation than the RF links. This behavior is attributed to the strong frequency dependence of soil conductivity, which disproportionately increases attenuation at higher RF frequencies. The observed trends are consistent with previously reported experimental and analytical models of underground wireless propagation, supporting the suitability of MI-based communication for short-range underground environments with elevated moisture levels.

To assess the robustness of the propagation model under varying soil conditions, a sensitivity analysis is presented in Figure 10b. Among the examined parameters (see Table 2), soil moisture content emerges as the dominant factor influencing path-loss variation, exceeding the impact of the sand fraction, burial depth, and soil composition parameters such as clay and silt content. This result underscores the critical role of the volumetric water content in determining soil dielectric properties and, consequently, electromagnetic wave propagation in underground environments. Even modest variations in moisture levels can therefore produce significant shifts in communication performance, emphasizing the need for adaptive system design in environments subject to seasonal or weather-induced soil changes.

Table 2. Parameters of underground sensor network (UGSN) scenario.

Parameter	Symbol/Value	Model/Notes
Frequency bands	100 MHz, 433 MHz, 868 MHz, 2.4 GHz, 24 GHz	RF propagation through soil (CRIM-based)
MI channel	20 MHz	Inductive coupling (coil model)
Soil moisture	0.15–0.35 (vol. fraction)	affects εr, σ via CRIM model
Soil texture	sand = 0.6, silt = 0.3, clay = 0.1	defines effective permittivity
Burial depth	0.2 m	attenuation increases with depth
Range	0.1–10 m (100 samples)	logarithmic sampling
Coil parameters	N = 20 turns, r = 0.05 m, Q = 50, alignment = 0.9	mutual inductance link
Antenna/coil gain	0 dBi each	isotropic assumption
Environmental factors	soil moisture, conductivity, texture	considered
Propagation model	CRIM + exponential path loss	used

3.2. Underwater Sensor Network Electromagnetic Propagation

In this scenario (see Table 3), the underwater electromagnetic channel is analyzed to examine how propagation loss varies with frequency. In the 10–100 MHz range, electromagnetic path loss increases approximately linearly with distance and exhibits only weak frequency dependence, owing to the relatively low conductivity of freshwater. Nevertheless, electromagnetic wave propagation in underwater environments supports high data-rate transmission only over very short ranges, typically below 1 m, due to rapid attenuation.

Table 3. Parameters of shallow water sensor network (SWSN) scenario.

Parameter	Symbol/Value	Model/Notes
EM carriers	10 MHz, 100 MHz, 433 MHz, 868 MHz, 2.4 GHz, 24 GHz	near-surface EM propagation
Range	0.1–100 m	logarithmic scale
Surface loss	0.5 dB/km	configurable
Bottom loss	0.3 dB/km	configurable
Temperature/salinity	fixed (T = 20 °C)	implicit in Thorp model
Factors considered	spreading loss, absorption, surface/bottom reflection	included
Model used	Acoustic TL(f) = 20 log r + α(f) r	validated with Thorp

3.3. In-Body Communication: Frequency Dependence and Absorption

In-body wireless communication presents significant challenges due to the strong interaction between electromagnetic waves and biological tissues. The following results examine how path loss, delay spread, and energy absorption vary as a function of the operating frequency and implantation depth (see Table 4). Figure 12a combines three complementary aspects of in-body channel behavior. The left column shows that path loss increases with both the frequency and implantation depth in the range of 5–50 mm, reflecting the strong absorption of electromagnetic waves by biological tissues, particularly above 2 GHz.

Table 4. Parameters of body area network (BAN) scenario.

Parameter	Symbol/Value	Model/Notes
Frequency sweep	0.5–6 GHz (400 pts)	wideband ABCD multilayer model
Layers	skin ($\varepsilon r \approx 40$), fat ($\varepsilon r \approx 6$), muscle ($\varepsilon r \approx 54$)	dispersive Cole–Cole
Depths	0–40 mm	sampling per 5 mm
Bands plotted	433 MHz, 868 MHz, 2.4 GHz, 5.8 GHz, 24 GHz	representative slices
Antenna gains	isotropic (0 dBi)	can be replaced
Environment	human body tissue (lossy)	homogeneous multilayer
Interpolation guard	active	warns if bands out of sweep
Output metrics	Path Loss vs. f, Depth; RMS-Delay Spread	computed analytically

Although the 2.36–2.4 GHz band is specified in IEEE 802.15.6 for medical body area networks, it was not included in the present simulations due to its propagation characteristics being representative of the broader 2.4 GHz ISM band already considered. Including both bands would not yield additional insight within the scope of the comparative analysis, while increasing result redundancy.

The middle column illustrates a reduction in the RMS delay spread with an increasing implantation depth, indicating diminished multipath contributions as wave propagation becomes increasingly dominated by absorption rather than reflection within tissue layers. The right column presents the relative specific absorption rate (SAR) distribution, which decreases with depth as electromagnetic energy is progressively absorbed along the propagation path.

Figure 12b further extends this analysis by illustrating the evolution of path loss across different operating frequencies and implantation depths. Results at 0.9 GHz, 2.4 GHz, 6 GHz, and 24 GHz show that, at lower frequencies, path loss remains within approximately 10–30 dB for depths below 30 mm, whereas at 24 GHz, the attenuation exceeds 300 dB, rendering millimeter-wave signals impractical for in-body wireless communication.

3.4. Indoor Propagation: Material Effects and Multi-Wall Modeling

The indoor scenario (see Table 5). examines millimeter-wave propagation at 24 GHz in a typical room environment, with an emphasis on the effects of distance, obstacles, and building materials. Walls within the simulated building are modeled as layered structures with varying thicknesses, enabling a realistic representation of multi-wall propagation effects.

Table 5. Parameters of indoor scenario.

Parameter	Symbol/Value	Model/Notes
Frequency	433 MHz, 868 MHz, 2.4 GHz, 24 GHz	Log-distance + Multi-wall
Range	1–50 m	typical room scale
Path-loss exponent	$N_{eff} \approx 1.8$–2.3	frequency-dependent per ITU P.1238
Shadowing (σ)	5 dB	log-normal
Walls	drywall × 3 (5 m), glass × 1 (12 m)	with variable spacing
RMS-DS base	25 ns	increases linearly with range
RMS-DS slope	0.5 ns/m	time-dispersion approximation
Frequency dependence	$N_{eff}(f) = N_0 + k \log_{10}(f/2.4\ \text{GHz})$	implemented
Factors considered	walls, materials, spacing, frequency dependence, shadowing	included
Model used	Multi-wall empirical and stochastic delay	used

Figure 13a presents three complementary characteristics of the 24 GHz indoor channel. The cumulative distribution function (CDF) of the received signal strength (RSS) indicates a mean received power of approximately −90 dBm. The RMS delay spread increases nearly linearly with distance, ranging from 15 ns to 45 ns, which reflects the growing contribution of multiple reflections under NLOS conditions. The right-hand panel summarizes material penetration losses, showing attenuation levels of approximately 21 dB for drywall and 5 dB for glass. These results are particularly relevant for practical indoor deployments at 24 GHz, as drywall and glass are commonly used construction materials.

Figure 13b illustrates path loss as a function of distance over the range 0–50 m, revealing distinct step-like increases whenever the signal traverses an additional wall. This behavior reflects realistic indoor propagation scenarios, where a receiver located in adjacent rooms experiences progressive signal degradation as the number of intervening walls increases.

To further investigate the influence of the building structure on indoor signal propagation, the following figures analyze the combined effects of the wall count and inter-wall spacing on path loss. Figure 14a presents a heatmap of the maximum path loss $d_{\max}$ as a function of the number of walls and the spacing between them. The results show a pronounced increase in path loss as the wall count increases, reaching values of approximately 160 dB, while inter-wall spacing exhibits a comparatively weaker influence.

To complete the indoor propagation analysis for wireless systems operating at 24 GHz, Figure 14b evaluates the sensitivity of the model to key parameters, including the wall count, effective refractive index (N_{eff}), inter-wall spacing, and shadowing standard deviation. Among these parameters, the number of walls and the effective refractive index emerge as the dominant factors governing indoor path-loss behavior and signal degradation, whereas spacing and shadowing variations have a secondary impact.

3.5. Outdoor mmWave Links

Outdoor propagation at 24 GHz is examined under LOS conditions, focusing on the variation of received signal power with distance (see Table 6). Specifically, a 24 GHz LOS link is evaluated over distances of up to 2 km. The RSS decreases monotonically with

distance, dropping from approximately −80 dBm at 100 m to −118 dBm at 2 km, illustrating the pronounced impact of path loss in outdoor millimeter-wave links.

Table 6. Parameters of outdoor scenario.

Parameter	Symbol/Value	Model/Notes
Frequencies	433 MHz, 868 MHz, 2.4 GHz, 24 GHz	multi-band sweep
Distance	50–2000 m	
Base height	h_b = 10 m	transmitter tower
Mobile height	h_m = 1.5 m	receiver terminal
Environment	urban	COST-231/Hata for ≤2 GHz; 3GPP 38.901 for >2 GHz
Transmit power	P_{tx} = 14 dBm	
Sensitivity	−120 dBm	detection limit
Foliage loss	0.02 dB/m (0–100 m depth)	optional
Calibration noise	σ = 3 dB, bias = 2 dB	synthetic measurement model
Antenna gains	$G_t = G_r$ = 0 dBi	isotropic
Factors considered	LOS/NLOS, foliage, calibration error, sensitivity	included
Model used	Hybrid COST-231/3GPP 38.901	used

The accompanying histogram of residuals demonstrates a clear improvement in model accuracy following the calibration step ("After calib"). Calibration is performed by adjusting the propagation model parameters to better match empirical RSS measurements. As shown in the histogram, post-calibration errors are more tightly centered around zero and exhibit reduced variance, indicating improved predictive performance of the calibrated model.

To complement this analysis, Figure 15b presents the path loss versus distance for an outdoor environment at 24 GHz, derived from the Friis free-space propagation model. As expected, the curve exhibits a steady increase in attenuation with distance, reflecting the fundamental propagation characteristics of millimeter-wave signals in unobstructed outdoor environments.

Since real-world urban propagation channels exhibit both deterministic and stochastic behavior, a probabilistic modeling framework is required for accurate representation. Figure 16 illustrates the 3GPP Urban Micro (UMi) path-loss model at 24.0 GHz, including both LOS and NLOS components. The gradual transition from LOS to NLOS dominated propagation with increasing distance reflecting realistic urban channel dynamics, where building density and obstructions progressively degrade signal quality.

The shaded regions surrounding each curve represent the corresponding statistical variation ($\pm\sigma$), while the dashed curve denotes the mean path loss, computed by weighting the LOS and NLOS components according to the distance-dependent LOS probability, $P_{\mathrm{LOS}}(d)$. This formulation captures both large-scale attenuation trends and shadowing effects characteristic of dense urban millimeter-wave deployments.

3.6. Trade-Offs Between Technologies

Figure 17 presents a Pareto-type analysis of latency versus energy consumption for underground communication systems. The plot illustrates feasible operating regions for RF-based soil propagation (50 kbps–1Mbps), magneto-inductive (MI) links (5–50 kbps), and acoustic links (0.5–5 kbps). The nearly horizontal trends indicate that latency is primarily governed by the achievable data rate, while the wide separation along the energy axis reflects the fundamentally different efficiency characteristics of each physical transmission

mechanism. This representation supports technology selection based on application-specific constraints, such as the available energy budget and latency tolerance.

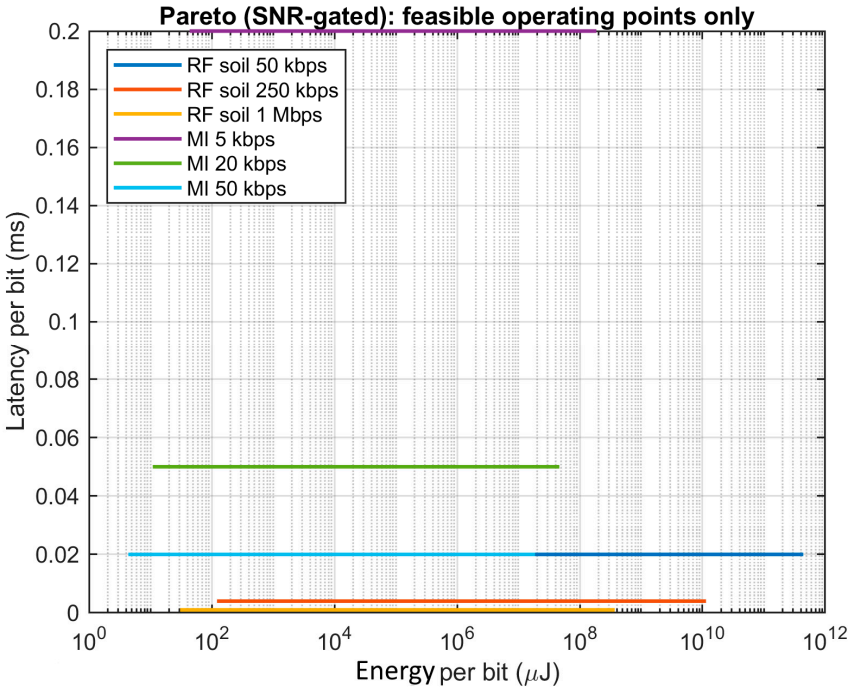

Figure 17. Pareto analysis of latency–energy trade-offs across physical media.

It is important to note that, while individual performance analyses of RF, magnetic induction, and acoustic communication links have been extensively reported in the literature, such evaluations are typically conducted in isolation and within technology-specific contexts. To the authors' knowledge, a unified Pareto-type comparison that jointly captures latency–energy trade-offs across fundamentally different physical transmission mechanisms and deployment media has not been previously reported in a consolidated and performance-oriented manner.

The proposed Pareto analysis therefore serves as a decision-oriented tool rather than a purely descriptive metric. By explicitly visualizing feasible operating regions, it enables system designers to rapidly assess the suitability of candidate communication technologies under application-specific constraints based on the energy budget, latency tolerance, and achievable data rate. This representation bridges the gap between propagation-level modeling and system-level technology selection for heterogeneous wireless sensor network deployments.

Overall, the presented results demonstrate that no single propagation model or communication mechanism is universally optimal across all deployment environments. Instead, performance is strongly governed by the physical properties of the propagation medium, operating frequency, and coupling mechanism. The comparative analysis highlights clear feasibility boundaries and trade-offs, providing practical insight into technology selection for environment-specific WSN deployments.

3.7. Model Validation, Applicability, and Limitations

The propagation models analyzed and compared in this work are grounded in a substantial body of experimentally validated studies reported in the open literature. For underground wireless sensor networks, soil-based electromagnetic and magnetic induction models have been supported by controlled laboratory measurements and field experiments under varying moisture and composition conditions, demonstrating strong agreement

between analytical predictions and observed attenuation trends. Similarly, submerged wireless sensor network models are based on experimentally characterized electromagnetic, magnetic induction, optical, and acoustic channels, with attenuation coefficients, absorption parameters, and multipath characteristics derived from freshwater and seawater measurement campaigns.

For body area networks, extensive experimental validation exists through tissue-equivalent phantom measurements, in vivo studies, and standardized channel models. The dielectric properties of biological tissues employed in this work are based on well-established Cole-Cole parameterizations, while in-body, on-body, and off-body propagation models have been experimentally verified across multiple frequency bands, including those adopted in the IEEE 802.15.6 standard. Indoor and outdoor propagation models considered in this paper are likewise supported by large-scale channel sounding campaigns, standardized empirical models, and measurement-driven statistical characterizations, including those used in contemporary cellular and IoT system design.

It is emphasized that the objective of this work is not to introduce new experimental campaigns, but rather to provide a unifying analytical and simulation-based framework that enables a consistent comparison across fundamentally different propagation environments. By relying on experimentally validated models reported in the literature and applying them under harmonized assumptions and metrics, the presented results highlight relative performance trends and feasibility limits across deployment scenarios.

Despite their proven utility, the considered models are subject to inherent limitations. Many analytical formulations assume homogeneous or piecewise-homogeneous media, isotropic or idealized antenna and coil characteristics, and stationary propagation conditions. Environmental variability, such as dynamic soil moisture changes, water turbulence, human motion, or temporal blockage, is typically captured only through statistical abstractions rather than fully dynamic modeling. In addition, certain models are valid only within specific frequency ranges or distance regimes, beyond which their accuracy may degrade.

These limitations do not diminish the comparative value of the presented framework but rather delineate its applicability boundaries. Future research directions include the integration of hybrid deterministic–statistical models, data-driven and learning-assisted channel characterization, and coordinated experimental campaigns spanning multiple propagation environments. Such efforts would further enhance the accuracy, adaptability, and generalizability of wireless sensor network propagation modeling.

4. Discussion

The results presented in Section 3 reveal distinct propagation behaviors across the examined deployment environments, driven by the underlying physical interaction between electromagnetic waves and the surrounding medium [75]. In underground scenarios, radio-frequency propagation is strongly constrained by the soil conductivity and moisture content, leading to rapid attenuation beyond short distances. Under these conditions, magneto-inductive transmission demonstrates increased robustness at ranges beyond approximately one meter, confirming its suitability for short-range underground sensing applications where conventional RF links become ineffective.

In submerged environments, electromagnetic propagation is shown to support only very short communication ranges due to conductive losses in water, particularly at higher frequencies. These findings reinforce the practical limitation of RF-based underwater links to short-range, high-data-rate applications and motivate the careful selection of the operating frequency and communication modality depending on deployment constraints. Acoustic communication, while referenced for a contextual comparison, operates under fun-

damentally different physical principles and is not the focus of the present electromagnetic modeling framework.

Body-centric communication results highlight the pronounced dependence of path loss and energy absorption on both the frequency and implantation depth. The results confirm that lower microwave frequencies enable feasible in-body communication over clinically relevant depths, whereas millimeter-wave operation leads to prohibitive attenuation and excessive absorption, rendering it impractical for implantable applications. For on-body and off-body scenarios, propagation is strongly influenced by the body geometry, movement, and polarization effects, consistent with statistical channel models reported in the literature.

Indoor propagation results demonstrate the sensitivity of millimeter-wave links to the building structure, particularly the wall count, material composition, and effective refractive index. The observed step-like increases in path loss with additional walls emphasize the importance of accurate material-aware modeling for indoor deployments. Outdoor results further confirm that deterministic free-space models alone are insufficient in urban environments, where stochastic effects associated with blockage and shadowing dominate. The agreement between simulated results and the 3GPP Urban Micro model validates the adopted probabilistic framework and its ability to capture realistic LOS—NLOS transitions.

Beyond environment-specific observations, the Pareto-based comparison highlights a more general insight: optimal communication technology selection in wireless sensor networks cannot be performed solely at the physical-layer level. Instead, it requires the joint consideration of propagation constraints, energy efficiency, and latency requirements. The presented framework provides a compact mechanism for such cross-layer reasoning, particularly in heterogeneous deployments where multiple physical media and transmission mechanisms may coexist.

Overall, the comparative analysis across environments illustrates that no single propagation model or communication strategy is universally optimal. Instead, each deployment scenario imposes distinct constraints on the achievable range, energy efficiency, and data rate, defining practical operating boundaries for system design. These findings provide a coherent basis for selecting appropriate electromagnetic propagation models and communication technologies in heterogeneous wireless sensor network deployments.

Recent literature has further advanced wireless sensor network propagation modeling through machine-learning-assisted channel characterization, environment-aware data-driven approaches, and extended experimental investigations at millimeter-wave and sub-terahertz frequencies. These studies demonstrate the growing role of hybrid analytical-learning frameworks and high-frequency measurements in capturing complex propagation dynamics, particularly in body-centric, indoor, and short-range high-capacity scenarios. While such approaches complement classical analytical models, they also highlight emerging research directions toward adaptive and data-informed propagation modeling for future WSN deployments [76–81].

In summary, the results across all examined environments confirm that the propagation behavior, achievable range, and energy efficiency are highly scenario-dependent. Underground and submerged deployments favor magnetic induction or low-frequency operation, in-body communication is dominated by absorption and SAR constraints, and indoor/outdoor systems benefit from higher-frequency operation when line-of-sight conditions are available. These findings reinforce the need for environment-aware model selection in WSN design.

5. Conclusions

This work presented a unified performance-oriented analysis of wireless sensor network communication across underground, submerged, body-centric, indoor, and outdoor

environments, covering a broad range of operating frequencies and electromagnetic propagation models. By systematically evaluating representative scenarios, the study highlighted the fundamental trade-offs among the achievable communication range, energy efficiency, and data rate that arise from the physical interaction between electromagnetic waves and the surrounding medium.

The results confirm that no single communication technology or frequency band is universally optimal across all deployment environments. Magneto-inductive transmission is shown to be well suited for short- to medium-range subsurface links, where conventional radio-frequency propagation is severely constrained by conductive losses. In contrast, RF and millimeter-wave links provide high data-rate connectivity in surface, near-surface, and open environments, but exhibit limited penetration capability and increased sensitivity to obstruction and material properties.

Quantitatively, the results show attenuation differences exceeding 40–80 dB between radiative and magnetic induction links in underground environments, absorption gradients of up to 1.5 dB/cm in in-body channels, and path-loss increases exceeding 150 dB in indoor millimeter-wave scenarios with multiple obstructions. These findings provide concrete guidance for frequency selection, communication modality choices, and deployment planning in heterogeneous WSNs.

A key outcome of this study is the reaffirmation that lower-frequency operation remains highly relevant for wireless sensor networks, despite the growing emphasis on high-frequency and millimeter-wave technologies in next-generation communication systems. Many sensor applications prioritize reliability, penetration capability, and energy efficiency over raw throughput. In challenging environments such as underground, submerged, or dense indoor settings, these requirements are more effectively satisfied by lower frequency operation.

Figure 18 presented at the end of this work provides a comparative overview of key design requirements across different wireless sensor network environments, namely underground, submerged, indoor, outdoor, and human body networks. The deformation of each polygon highlights how the relative importance of channel conditions, energy constraints, reliability demands, and deployment challenges varies significantly depending on the operating medium.

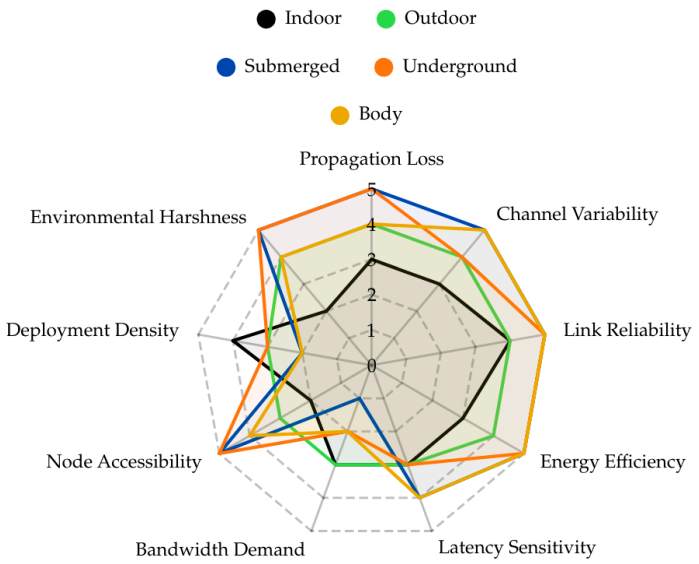

Figure 18. Weights of metrics for WSN environments.

The proposed analysis framework and results provide a coherent reference for system designers, enabling informed selection of communication technologies and operating frequencies based on environmental constraints and application requirements. Future work may extend this framework toward adaptive and hybrid communication strategies that dynamically adjust operating parameters in response to changing propagation conditions and network demands.

Author Contributions: Conceptualization, T.N.F.K.; methodology, A.G., N.K., I.G. and T.N.F.K.; investigation, A.G., N.K., I.G. and T.N.F.K.; resources, A.G., N.K., I.G. and T.N.F.K.; writing—original draft preparation, A.G., N.K., I.G. and T.N.F.K.; writing—review and editing, A.G., N.K., I.G. and T.N.F.K.; visualization, A.G., N.K., I.G. and T.N.F.K.; supervision, T.N.F.K.; project administration, T.N.F.K. All authors have read and agreed to the published version of the manuscript.

Funding: This research received no external funding.

Data Availability Statement: All data generated or analyzed during this study are included in this published article.

Conflicts of Interest: The authors declare no conflict of interest.

Abbreviations

The following abbreviations are used in this manuscript:

5G NR	5G New Radio
AG-UG	Above-Ground to Underground
AWGN	Additive White Gaussian Noise
BAN	Body Area Network
CDF	Cumulative Distribution Function
CNN	Convolutional Neural Network
CRIM-Fresnel	Complex Refractive Index Model with Fresnel corrections
EM	ElectroMagnetic
FDTD	Finite Difference Time Domain
FSPL	Basic Free Space Path Loss
GO	Geometrical Optics
ISM	Industrial Scientific and Medical
LCP	Liquid Crystal Polymer
LOS	Line of Sight
MAC	Medium Access Control
MI	Magnetic Induction
NLOS	Non Line of Sight
RF	Radio Frequency
RMS	Root Mean Square
RSS	Received Signal Strength
SAR	Specific Absorption Rate
SOFAR	Sound Fixing and Ranging
SWSN	Submerged Wireless Sensor Networks
UG-AG	Underground to Above Ground
UGSN	Underground Wireless Sensor Networks
UG-UG	Underground to Underground
UMi	Urban Micro
UWB	Ultra-Wideband
WSN	Wireless Sensor Network
WUSN	Wireless Underground Sensor Network

References

1. Jamshed, M.A.; Ali, K.; Abbasi, Q.H.; Imran, M.A.; Ur-Rehman, M. Challenges, Applications, and Future of Wireless Sensors in Internet of Things: A Review. *IEEE Sens. J.* **2022**, *22*, 5482–5494. [CrossRef]
2. Zhang, H.; Li, B.; Karimi, M.; Saydam, S.; Hassan, M. Recent Advancements in IoT Implementation for Environmental, Safety, and Production Monitoring in Underground Mines. *IEEE Internet Things J.* **2023**, *10*, 14507–14526. [CrossRef]
3. Etman, A.M.; Abdalzaher, M.S.; Emran, A.A.; Yahya, A.; Shaaban, M. A Survey on Machine Learning Techniques in Smart Grids Based on Wireless Sensor Networks. *IEEE Access* **2025**, *13*, 2604–2627. [CrossRef]
4. Islam, T.; Park, S.-H. A Comprehensive Survey of the Recently Proposed Localization Protocols for Underwater Sensor Networks. *IEEE Access* **2020**, *8*, 179224–179243. [CrossRef]
5. Banaseka, F.K.; Katsriku, F.; Abdulai, J.D.; Adu-Manu, K.S.; Engmann, F.N.A. Signal Propagation Models in Soil Medium for the Study of Wireless Underground Sensor Networks: A Review of Current Trends. *Wirel. Commun. Mob. Comput.* **2021**, *2021*, 8836426. [CrossRef]
6. Abdorahimi, D.; Sadeghioon, A.M. Comparison of radio frequency path loss models in soil for wireless underground sensor networks. *J. Sens. Actuator Netw.* **2019**, *8*, 35. [CrossRef]
7. Vuran, M.C.; Akyildiz, I.F. Channel model and analysis for wireless underground sensor networks in soil medium. *Phys. Commun.* **2010**, *3*, 245–254. [CrossRef]
8. Bogena, H.R.; Huisman, J.A.; Meier, H.; Rosenbaum, U.; Weuthen, A. Hybrid wireless underground sensor networks: Quantification of signal attenuation in soil. *Vadose Zone J.* **2009**, *8*, 755–761. [CrossRef]
9. Peplinski, N.; Ulaby, F.; Dobson, M. Dielectric properties of soils in the 0.3–1.3 GHz range. *IEEE Trans. Geosci. Remote Sens.* **1995**, *33*, 803–807. [CrossRef]
10. Chaamwe, N.; Liu, W.; Jiang, H. Wave propagation communication models for Wireless Underground Sensor Networks. In Proceedings of the 2010 IEEE 12th International Conference on Communication Technology, Nanjing, China, 11–14 November 2010. [CrossRef]
11. Orphanides, S.J. *Electromagnetic Waves and Antennas*; Example 4.5.3.; Rutgers University: New Brunswick, NJ, USA, 2008.
12. Yun, Z.; Iskander, M.F. Ray Tracing for Radio Propagation Modeling: Principles and Applicationss. *IEEE Access* **2015**, *3*, 1089–1100. [CrossRef]
13. Ruan, H.; Zhang, Z.; Ma, H.; Xing, Z. Physics-Informed Multi-View Neural Surface Reconstruction in Wireless Networks. In Proceedings of the 2025 IEEE 26th International Workshop on Signal Processing and Artificial Intelligence for Wireless Communications (SPAWC), Surrey, UK, 7–10 July 2025. [CrossRef]
14. King, R.W.; Owens, M.; Wu, T.T. *Lateral Electromagnetic Waves, Theory and Applications to Communications, Geophysical Exploration, and Remote Sensing*; Springer: Heidelberg/Berlin, Germany, 1992; ISBN 13: 9780387976792.
15. Dong, X.; Vuran, M.C. A Channel Model for Wireless Underground Sensor Networks Using Lateral Waves. In Proceedings of the 2011 IEEE Global Telecommunications Conference—GLOBECOM 2011, Houston, TX, USA, 5–9 December 2011; pp. 1–6. [CrossRef]
16. Felsen, L.B.; Marcuvitz, N. *Radiation and Scattering of Waves*; Wiley-IEEE Press: Hoboken, NJ, USA, 1994; ISBN 978-0-780-31088-9.
17. Belaid, H.; Mostarshedi, S.; Poussot, B.; Laheurte, J.-M. Accurate Estimation of the Lateral Wave's Contribution to the Radiated Fields of a Vertical Electric Dipole Embedded in a Lossy Half-Space. *IEEE Trans. Antennas Propag.* **2024**, *72*, 8709–8718. [CrossRef]
18. Pathak, P.H.; Burkholder, R.J. *Electromagnetic Radiation, Scattering, and Diffraction*; Wiley-IEEE Press: Hoboken, NJ, USA, 2021; ISBN 978-1-119-81051-3.
19. Norton, K.A. The propagation of radio waves over the surface of the earth and in the upper atmosphere. *Proc. IRE* **1936**, *24*, 1367–1387. [CrossRef]
20. Silva, B.; Fisher, R.M.; Kumar, A.; Hancke, G.P. Experimental Link Quality Characterization of Wireless Sensor Networks for Underground Monitoring. *IEEE Trans. Ind. Inform.* **2015**, *11*, 1099–1110. [CrossRef]
21. Cardoso, M.H.B.; Mostarshedi, S.; Baudoin, G.; Laheurte, J.-M. Analytical Expressions of Critical Distances for Near-Ground Propagation. *IEEE Trans. Antennas Propag.* **2018**, *66*, 2482–2493. [CrossRef]
22. Karkanis, N.; Giannakoulas, A.; Kyriacou, G.; Kaifas, T. Near Field Focusing to Assist Emerging Networking, Tracking and Sensing. In Proceedings of the IEEE 6th International Conference on Communications, Information, Electronic and Energy Systems—CIEES 2024, Ruse, Bulgaria, 26–28 November 2025.
23. Giannakoulas, A.; Karkanis, N.; Markou, S.; Kyriacou, G.; Kaifas, T. Sidelink Communication for Unmanned Platforms' (UxU) Swarms in Challenging Scenarios. In Proceedings of the IEEE 6th International Conference on Communications, Information, Electronic and Energy Systems—CIEES 2024, Ruse, Bulgaria, 26–28 November 2025.
24. Reddy, T.P.; Kumar, C.S.; Suman, K.; Avinash, U.; Kuresan, H. Wireless Underground Sensor Network Using Magnetic Induction. In Proceedings of the 2020 International Conference on Communication and Signal Processing (ICCSP), Chennai, India, 28–30 July 2020; pp. 1394–1398. [CrossRef]

25. Silva, A.R.; Moghaddam, M. Operating frequency selection for low-power magnetic induction-based wireless underground sensor networks. In Proceedings of the 2015 IEEE Sensors Applications Symposium (SAS), Zadar, Croatia, 13–15 April 2015; pp. 1–6. [CrossRef]
26. Deng, S.; Liu, G.; Chen, Z.; Zhang, H.; Jiang, T. Channel modeling for MI-based wireless underground sensor networks with conductive objects. *Sci. China Inf. Sci.* **2024**, *67*, 179302. [CrossRef]
27. Kisseleff, S.; Akyildiz, I.F.; Gerstacker, W.H. Survey on Advances in Magnetic Induction-Based Wireless Underground Sensor Networks. *IEEE Internet Things J.* **2018**, *5*, 4843–4856. [CrossRef]
28. Muzzammil, M.; Ahmed, N.; Qiao, G.; Ullah, I.; Wan, L. Fundamentals and Advancements of Magnetic-Field Communication for Underwater Wireless Sensor Networks. *IEEE Trans. Antennas Propag.* **2020**, *68*, 7555–7570. [CrossRef]
29. Davis, A.; Chang, H. Underwater wireless sensor networks. In Proceedings of the 2012 Oceans, Hampton Roads, VA, USA, 14–19 October 2012; pp. 1–5. [CrossRef]
30. Buchanan, K.R.; Manzano-Roth, R.; Lin, A.; Loaiza, G.; Sills, M.; Li, J.; Wheeland, S.R.; Chakrabarti, S.; Rodriguez, A.R.; Huff, G.H.; et al. Investigation of Randomly Populated Cylindrical, Spherical, and Cubical Arrays for Application in Space, Aerial, and Underwater Collaborative Beamforming. *IEEE Access* **2024**, *12*, 171944–171971. [CrossRef]
31. Petzold, T.J. *Volume Scattering Functions for Selected Ocean Waters*; Paper SIO Reference 72–78; Scripps Institute of Oceanography: La Jolla, CA, USA, 1972.
32. Jerlov, N.G. *Optical Oceanography*; Elsevier Oceanography Series; Elsevier Publishing Company: Amsterdam, The Netherlands, 1968; ISBN 978-0-444-40320-9.
33. Quan, X.; Fry, E.S. Empirical equation for the index of refraction of seawater. *Appl. Opt.* **1995**, *34*, 3477–3480. [CrossRef]
34. Haltrin, V.I. Chlorophyll-based model of seawater optical properties. *Appl. Opt.* **1999**, *38*, 6826–6832. [CrossRef]
35. Fang, C.; Li, S.; Wang, K. Accurate Underwater Optical Wireless Communication Model with Both Line-of-Sight and Non-Line-of-Sight Channels. *IEEE Photon- J.* **2022**, *14*, 7358312. [CrossRef]
36. Jaruwatanadilok, S. Underwater Wireless Optical Communication Channel Modeling and Performance Evaluation using Vector Radiative Transfer Theory. *IEEE J. Sel. Areas Commun.* **2008**, *26*, 1620–1627. [CrossRef]
37. Saeed, N.; Celik, A.; Al-Naffouri, T.Y.; Alouini, M.-S. Underwater optical wireless communications, networking, and localization: A survey. *Ad Hoc Netw.* **2019**, *94*, 101935. [CrossRef]
38. Ning, X.; Winston, R.; O'Gallagher, J. Dielectric totally internally reflecting concentrators. *Appl. Opt.* **1987**, *26*, 300–305. [CrossRef]
39. Kedar, D.; Arnon, S. Non-line-of-sight optical wireless sensor network operating in multiscattering channel. *Appl. Opt.* **2006**, *45*, 8454–8461. [CrossRef]
40. Arnon, S. Underwater optical wireless communication network. *Opt. Eng.* **2010**, *49*, 015001-1–015001-6. [CrossRef]
41. Kou, L.; Yan, S.; Liu, J.; Zhang, J.; Leng, J.; Wang, J.; An, R. The Investigation of Underwater Wireless Optical Communication Channel Fading in Multisize Particles, Bubbles, and Turbulence. *IEEE Internet Things J.* **2025**, *12*, 52293–52307. [CrossRef]
42. Zedini, E.; Ata, Y.; Al-Sallami, F.M.; Rajbhandari, S. Evaluation of Underwater Optical Wireless Channels Over F Turbulence for Different Detection Types. *IEEE Trans. Commun.* **2025**, *73*, 1925–1937. [CrossRef]
43. Zayed, M.M.; Shokair, M. Performance analysis and optimization of modulation techniques for underwater optical wireless communication in varied aquatic environments. *Sci. Rep.* **2025**, *15*, 32570. [CrossRef]
44. Praharsha, S.P.; Miriyala, M. Emerging Concepts for Revolutionizing Underwater Visible Light Communication: A Review. *IEEE Access* **2025**, *13*, 185943–185972. [CrossRef]
45. Stojanovic, M.; Preisig, J. Underwater acoustic communication channels: Propagation models and statistical characterization. *IEEE Commun. Mag.* **2009**, *47*, 84–89. [CrossRef]
46. Thorp, W.H. Deep-ocean sound attenuation in the sub-and low-kilocycle-per-second region. *J. Acoust. Soc. Am.* **1965**, *38*, 648–654. [CrossRef]
47. Brekhovskikh, L.M.; Lysanov, Y.P. *Fundamentals of Ocean Acoustics*; Springer: Heidelberg/Berlin, Germany, 2003.
48. Qarabaqi, P.; Stojanovic, M. Statistical Characterization and Computationally Efficient Modeling of a Class of Underwater Acoustic Communication Channels. *IEEE J. Ocean. Eng.* **2013**, *38*, 701–717. [CrossRef]
49. Gabriel, S.; Lau, R.W.; Gabriel, C. The dielectric properties of biological tissues: III. Parametric models for the dielectric spectrum of tissues. *Phys. Med. Biol.* **1996**, *41*, 2271–2293. [CrossRef]
50. Chavez-Santiago, R.; Garcia-Pardo, C.; Fornes-Leal, A.; Valles-Lluch, A.; Vermeeren, G.; Joseph, W.; Balasingham, I.; Cardona, N. Experimental Path Loss Models for In-Body Communications within 2.36-2.5 GHz. *IEEE J. Biomed. Health Inform.* **2015**, *19*, 930–937. [CrossRef]
51. Chavez-Santiago, R.; Sayrafian-Pour, K.; Khaleghi, A.; Takizawa, K.; Wang, J.; Balasingham, I.; Li, H.-B. Propagation models for IEEE 802.15.6 standardization of implant communication in body area networks. *IEEE Commun. Mag.* **2013**, *51*, 80–87. [CrossRef]
52. Fort, A.; Desset, C.; Ryckaert, J.; De Doncker, P.; Van Biesen, L.; Wambacq, P. Characterization of the Ultra Wideband Body Area Propagation Channel. In Proceedings of the 2005 IEEE International Conference on Ultra-Wideband, Zurich, Switzerland, 5–8 September 2005; pp. 22–27. [CrossRef]

53. Demir, A.F.; Ankarali, Z.E.; Liu, Y.; Abbasi, Q.H.; Qaraqe, K.; Serpedin, E.; Arslan, H.; Gitlin, R.D. In Vivo Wireless Channel Modeling. *arXiv* **2019**. [CrossRef]
54. Zahid, M.; Shoaib, S.; Ilyas, A.; Sarwar, R.; Rehman, O.U.; Amin, Y. Flexible High-Gain Implantable Antenna for Biomedical Applications: Design and Performance Analysis. In Proceedings of the IEEE EUROCON 2025—21st International Conference on Smart Technologies, Gdynia, Poland, 4–6 June 2025; pp. 1–6. [CrossRef]
55. Liu, L.; Shi, J.; Han, F.; Tang, X.; Wang, J. In-Body to on-Body Channel Characterization and Modeling Based on Heterogeneous Human Models at HBC-UWB Band. *IEEE Sensors J.* **2022**, *22*, 19772–19785. [CrossRef]
56. Ferguson, J.E.; Redish, A.D. Wireless communication with implanted medical devices using the conductive properties of the body. *Expert Rev. Med. Devices* **2011**, *8*, 427–433. [CrossRef]
57. Movassaghi, S.; Abolhasan, M.; Lipman, J.; Smith, D.; Jamalipour, A. Wireless Body Area Networks: A Survey. *IEEE Commun. Surv. Tutor.* **2014**, *16*, 1658–1686. [CrossRef]
58. Behera, T.M.; Samal, U.C.; Mohapatra, S.K.; Khan, M.S.; Appasani, B.; Bizon, N.; Thounthong, P. Energy-Efficient Routing Protocols for Wireless Sensor Networks: Architectures, Strategies, and Performance. *Electronics* **2022**, *11*, 2282. [CrossRef]
59. Cotton, S.L.; Scanlon, W.G. Channel Characterization for Single- and Multiple-Antenna Wearable Systems Used for Indoor Body-to-Body Communications. *IEEE Trans. Antennas Propag.* **2009**, *57*, 980–990. [CrossRef]
60. Cheffena, M. Time-varying on-body wireless channel model during walking. *EURASIP J. Wirel. Commun. Netw.* **2014**, *2014*, 29. [CrossRef]
61. Pellegrini, A.; Brizzi, A.; Zhang, L.; Ali, K.; Hao, Y.; Wu, X.; Constantinou, C.C.; Nechayev, Y.; Hall, P.S.; Chahat, N.; et al. Antennas and Propagation for Body-Centric Wireless Communications at Millimeter-Wave Frequencies: A Review [Wireless Corner]. *IEEE Antennas Propag. Mag.* **2013**, *55*, 262–287. [CrossRef]
62. Mitsalas, X.M.; Kaifas, T.; Kyriacou, G.A. Space and leaky wave radiation from highly lossy biological cylindrical human-limps models. *Prog. Electromagn. Res. B* **2021**, *94*, 145–174. [CrossRef]
63. Mitsalas, X.M.; Kaifas, T.; Kyriacou, G.A. Wiener-hopf analysis of planar canonical structures loaded with longitudinally magnetized plasma biased normally to the extraordinarywave propagation: Near and far field. *Prog. Electromagn. Res. B* **2020**, *88*, 119–149. [CrossRef]
64. Shon, A.; Chu, J.-U.; Jung, J.; Kim, H.; Youn, I. An Implantable Wireless Neural Interface System for Simultaneous Recording and Stimulation of Peripheral Nerve with a Single Cuff Electrode. *Sensors* **2017**, *18*, 1. [CrossRef] [PubMed]
65. Samimi, M.K.; Rappaport, T.S. 3-D Millimeter-Wave Statistical Channel Model for 5G Wireless System Design. *IEEE Trans. Microw. Theory Tech.* **2016**, *64*, 2207–2225. [CrossRef]
66. Zakeri, H.; Khoddami, P.; Moradi, G.; Alibakhshikenari, M.; Abd-Alhameed, R.; Koziel, S.; Dalarsson, M. Path Loss Model Estimation at Indoor Environment by Using Deep Neural Network and CatBoost for Wireless Application. *IEEE Access* **2024**, *12*, 159070–159085. [CrossRef]
67. Seidel, S.Y.; Rappaport, T.S. 914 MHz path loss prediction models for indoor wireless communications in multifloored buildings. *IEEE Trans. Antennas Propag.* **1992**, *40*, 207–217. [CrossRef]
68. Hashemi, H. The indoor radio propagation channel. *Proc. IEEE* **1993**, *81*, 943–968. [CrossRef]
69. Briso, C.; Calvo, C.; Xu, Y. UWB Propagation Measurements and Modelling in Large Indoor Environments. *IEEE Access* **2019**, *7*, 41913–41920. [CrossRef]
70. Li, X.; Liu, R.; Xu, S.; Razul, S.G.; Yuen, C. TransPathNet: A Novel Two-Stage Framework for Indoor Radio Map Prediction. *arXiv* **2025**, arXiv:2501.16023. [CrossRef]
71. Patwari, N.; Wilson, J. RF Sensor Networks for Device-Free Localization: Measurements, Models, and Algorithms. *Proc. IEEE* **2010**, *98*, 1961–1973. [CrossRef]
72. Rappaport, T.S. *Wireless Communications: Principles and Practice*, 2nd ed.; Cambridge University Press: Cambridge, UK, 2024.
73. Goldsmith, A. *Wireless Communications*, 1st ed.; Cambridge University Press: Cambridge, UK, 2005. [CrossRef]
74. Nassef, L.; Elhebshi, R.; Jose, L. Evaluating Performance of Wireless Sensor Network in Realistic Smart Grid Environment. *Int. J. Wirel. Mob. Networks* **2018**, *10*, 27–36. [CrossRef]
75. Kaifas, T.N.F. Electromagnetic Power Harvesting by Electrically Small, Resonant, Parasitic, Superdirective Arrays Designed via Characteristic Mode Theory. In Proceedings of the 2024 5th International Conference on Communications, Information, Electronic and Energy Systems (CIEES), Veliko Tarnovo, Bulgaria, 20–22 November 2024; pp. 1–6. [CrossRef]
76. Galvan-Tejada, G.M.; Martinez-Enriquez, A.M. A machine learning scheme to assess the radio propagation conditions on wireless communication networks. *J. Ambient. Intell. Humaniz. Comput.* **2025**, *16*, 789–802. [CrossRef]
77. Alipio, M. Improving WSN-based dataset using data augmentation for TSCH protocol performance modeling. *Futur. Gener. Comput. Syst.* **2025**, *163*, 107540. [CrossRef]
78. Fondo-Ferreiro, P.; López-Bravo, C.; González-Castaño, F.J.; Gil-Castiñeira, F.; Candal-Ventureira, D. Learning-based visibility prediction for terahertz communications in 6G networks. *Comput. Commun.* **2024**, *228*, 107956. [CrossRef]

79. Bodet, D.; Petrov, V.; Petrushkevich, S.; Jornet, J.M. Sub-terahertz near field channel measurements and analysis with beamforming and Bessel beams. *Sci. Rep.* **2024**, *14*, 19675. [CrossRef] [PubMed]
80. Das, V.; Nahar, T.; Rawat, S. Survey of challenges, development, and potential tera-wave wearable antennas for wireless body area networks. *EURASIP J. Wirel. Commun. Netw.* **2025**, *2025*, 78. [CrossRef]
81. Zhang, X.; Liu, C.; Cheng, Y.; Li, Z.; Xu, C.; Huang, C.; Zhan, Y.; Bo, W.; Xia, J.; Xu, W. A Comprehensive Survey of Research Trends in mmWave Technologies for Medical Applications. *Sensors* **2025**, *25*, 3706. [CrossRef] [PubMed]

Disclaimer/Publisher's Note: The statements, opinions and data contained in all publications are solely those of the individual author(s) and contributor(s) and not of MDPI and/or the editor(s). MDPI and/or the editor(s) disclaim responsibility for any injury to people or property resulting from any ideas, methods, instructions or products referred to in the content.